

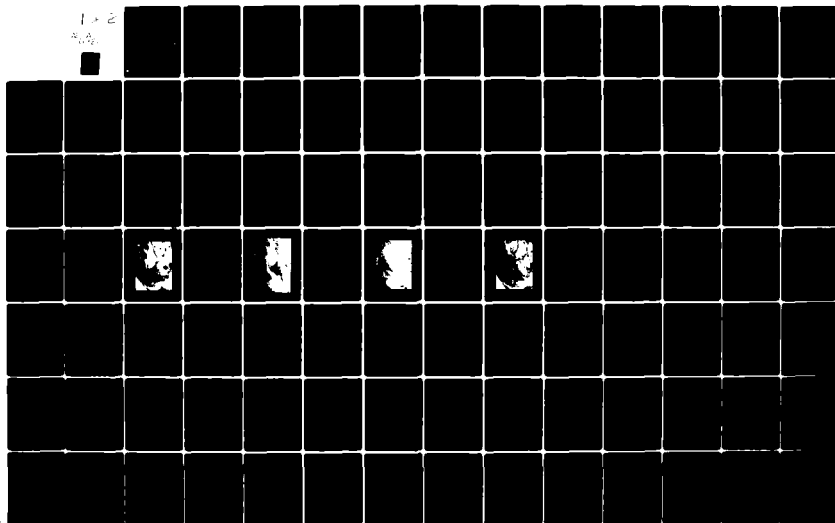
AD-A092 217

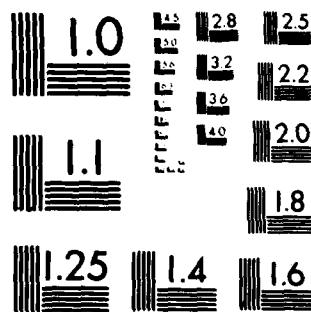
AIR FORCE INST OF TECH WRIGHT-PATTERSON AFB OH F/O 4/2
THE INFLUENCE OF CLOUD AND ATMOSPHERIC MOISTURE ON THE STATISTI--ETC(U)
AUG 80 P M SPECK
AFIT-CI-80-43T

UNCLASSIFIED

NL

1-2
AUG 80





MICROCOPY RESOLUTION TEST CHART
NATIONAL BUREAU OF STANDARDS-1963-A

AD A092217

14

UNCLASS

SECURITY CLASSIFICATION OF THIS PAGE (When Data Entered)

12, 129

AF

DTIC

REPORT DOCUMENTATION PAGE

READ INSTRUCTIONS
BEFORE COMPLETING FORM

1. REPORT NUMBER

80-43T

2. GOVT ACCESSION NO.

AD A092217

3. RECIPIENT'S CATALOG NUMBER

4. TITLE (and Subtitle)

The Influence of Cloud and
Atmospheric Moisture on the Statistical
Analysis of Nimbus VI Multispectral
Radiation Measurements.

5. TYPE OF REPORT & PERIOD COVERED

THESIS/DISSERTATION

6. PERFORMING ORG. REPORT NUMBER

7. AUTHOR(s)

10
Capt Peter Werner/Speck

8. CONTRACT OR GRANT NUMBER(s)

9. PERFORMING ORGANIZATION NAME AND ADDRESS

AFIT STUDENT AT: The University of Utah

10. PROGRAM ELEMENT PROJECT, TASK
AREA & WORK UNIT NUMBERS

11. CONTROLLING OFFICE NAME AND ADDRESS

AFIT/NR
WPAFB OH 45433

12. REPORT DATE

1980

13. NUMBER OF PAGES

114

14. MONITORING AGENCY NAME & ADDRESS (if different from Controlling Office)

9 Master's thesis

15. SECURITY CLASS. (of this report)

UNCLASS

15a. DECLASSIFICATION DOWNGRADING
SCHEDULE

16. DISTRIBUTION STATEMENT (of this Report)

APPROVED FOR PUBLIC RELEASE; DISTRIBUTION UNLIMITED

17. DISTRIBUTION STATEMENT (of the abstract entered in Block 20, if different from Report)

18. SUPPLEMENTARY NOTES

APPROVED FOR PUBLIC RELEASE: IAW AFR 190-17

Fredric C. Lynch
FREDRIC C. LYNCH, Major, USAF
Director of Public AffairsAir Force Institute of Technology (ATC)
Wright-Patterson AFB, OH 45433

19. KEY WORDS (Continue on reverse side if necessary and identify by block number)

20. ABSTRACT (Continue on reverse side if necessary and identify by block number)

ATTACHED

8011 24 162

DD FORM 1 JAN 73 1473

EDITION OF 1 NOV 65 IS OBSOLETE

UNCLASS

SECURITY CLASSIFICATION OF THIS PAGE (When Data Entered)

012200 Jm

BDC FILE COPY

SC 437

THE INFLUENCE OF CLOUD AND ATMOSPHERIC MOISTURE
ON THE STATISTICAL ANALYSIS OF NIMBUS VI
MULTISPECTRAL RADIATION MEASUREMENTS

by

Peter Werner Speck

A thesis submitted to the faculty of The
University of Utah in partial fulfillment of the requirements
for the degree of

Master of Science

Department of Meteorology

The University of Utah

August 1980

Available For	
DTIC TAB	<input checked="checked" type="checkbox"/>
Unannounced	<input type="checkbox"/>
Justification	
By	
Distribution	
Availability Codes	
Dist	Special
A	

Copyright © Peter W. Speck 1980

All Rights Reserved

457

The purpose of this questionnaire is to ascertain the value and/or contribution of research accomplished by students or faculty of the Air Force Institute of Technology (ATC). It would be greatly appreciated if you would complete the following questionnaire and return it to:

AFIT/NR
Wright-Patterson AFB OH 45433

Research Title: The Influence of Cloud and Atmospheric Moisture on
the Statistical Analysis of Nimbus VI Multispectral Radiation

Measurements
Author: Capt Peter Werner Speck

Research Assessment Questions:

1. Did this research contribute to a current Air Force project?

a. Yes b. No

2. Do you believe this research topic is significant enough that it would have been researched (or contracted) by your organization or another agency if AFIT had not?

a. Yes **b. No**

3. The benefits of AFIT research can often be expressed by the equivalent value that your agency achieved/received by virtue of AFIT performing the research. Can you estimate what this research would have cost if it had been accomplished under contract or if it had been done in-house in terms of manpower and/or dollars?

a.	Man-years	b.	\$
1.	10	10	10
2.	20	20	20
3.	30	30	30
4.	40	40	40
5.	50	50	50
6.	60	60	60
7.	70	70	70
8.	80	80	80
9.	90	90	90
10.	100	100	100

4. Often it is not possible to attach equivalent dollar values to research, although the results of the research may, in fact, be important. Whether or not you were able to establish an equivalent value for this research (3 above), what is your estimate of its significance?

2. Highly Significant	b. Significant	c. Slightly Significant	d. Of No Significance
1. 100%	1. 100%	1. 100%	1. 100%
2. 90%	2. 90%	2. 90%	2. 90%
3. 80%	3. 80%	3. 80%	3. 80%
4. 70%	4. 70%	4. 70%	4. 70%
5. 60%	5. 60%	5. 60%	5. 60%
6. 50%	6. 50%	6. 50%	6. 50%
7. 40%	7. 40%	7. 40%	7. 40%
8. 30%	8. 30%	8. 30%	8. 30%
9. 20%	9. 20%	9. 20%	9. 20%
10. 10%	10. 10%	10. 10%	10. 10%
11. 0%	11. 0%	11. 0%	11. 0%

5. AFIT welcomes any further comments you may have on the above questions, or any additional details concerning the current application, future potential, or other value of this research. Please use the back of this questionnaire for your statement(s).

NAME	GRADE	POSITION
------	-------	----------

ORGANIZATION	LOCATION
--------------	----------

USAF SCN 75-2011

THE UNIVERSITY OF UTAH GRADUATE SCHOOL

SUPERVISORY COMMITTEE APPROVAL

of a thesis submitted by

Peter Werner Speck

I have read this thesis and have found it to be of satisfactory quality for a master's degree.

June 5, 1980
Date

Elford G. Astling
Elford G. Astling
Chairman, Supervisory Committee

I have read this thesis and have found it to be of satisfactory quality for a master's degree.

June 5, 1980
Date

Kuo-Nan Liou
Kuo-Nan Liou
Member, Supervisory Committee

I have read this thesis and have found it to be of satisfactory quality for a master's degree.

6/5/80
Date

Julia N. Paegle
Julia N. Paegle
Member, Supervisory Committee

THE UNIVERSITY OF UTAH GRADUATE SCHOOL

FINAL READING APPROVAL

To the Graduate Council of The University of Utah:

I have read the thesis of Peter Werner Speck in its final form and have found that (1) its format, citations, and bibliographic style are consistent and acceptable; (2) its illustrative materials including figures, tables, and charts are in place; and (3) the final manuscript is satisfactory to the Supervisory Committee and is ready for submission to the Graduate School.

July 28, 1980
Date

Elford G. Astling
Elford G. Astling
Member, Supervisory Committee

Approved for the Major Department

S. K. Kao
S. K. Kao
Chairman Dean

Approved for the Graduate Council

James L. Clayton
Dean of The Graduate School

ABSTRACT

A study of the earth-atmosphere system with multispectral remote sensing measurements from Nimbus VI satellite was carried out over the North American continent when a mid-latitude cyclone was present. Correlative information between such conventional meteorological parameters as clouds, precipitation, atmospheric temperature, snow cover, and soil moisture was made with measurements from the SCAMS, ESMR, and HIRS experiments on Nimbus VI.

The results showed SCAMS microwave measurements were most sensitive to atmospheric parameters such as temperature and precipitating clouds while ESMR microwave measurements were dependent on surface conditions especially snow cover and soil moisture. Infrared and reflected solar radiance measurements from HIRS were useful in identifying cloud areas with conventional meteorological data.

TABLE OF CONTENTS

ABSTRACT	iv
LIST OF FIGURES	vi
LIST OF TABLES	ix
ACKNOWLEDGEMENTS	xii
CHAPTER	
I. INTRODUCTION	1
II. DATA SOURCES AND SYNOPTIC SITUATION	3
Nimbus VI Satellite Data	3
Conventional Meteorological Observations	17
GOES Visible and Infrared Imagery	17
Synoptic Situation	17
III. ANALYSIS PROCEDURE	36
Data Availability	36
Computation and Presentation of Results	41
IV. RESULTS	46
Surface, Cloud and Precipitation Effects on SCAMS Measurements	49
Terrain Effects on Data from SCAMS	67
Diurnal Temperature Variations in SCAMS Measurements	69
Comparisons of SCAMS, ESMR and HIRS Measurements	73
V. SUMMARY	91
Appendices	
A. THE DATA	94
B. SAMPLE CORRELATION COEFFICIENT ARRAYS	104
REFERENCES	112
VITA	114

LIST OF FIGURES

<u>Figure</u>	<u>Page</u>
2.1. SCAMS Weighting Function according to <u>Nimbus VI Users Guide</u> (1975)	7
2.2. SCAMS scan point locations at 1815 GMT 21 February 1976	9
2.3. ESMR scan point locations for a subsection of Nimbus VI orbital pass over northern Utah on 21 February 1976	11
2.4. Subjective analysis of average brightness temperatures ($^{\circ}\text{K}$) obtained from ESMR at 1815 GMT 21 February 1976	11
2.5. Objectively analyzed average brightness temperatures ($^{\circ}\text{K}$) from ESMR for a $1/2^{\circ}$ latitude-longitude grid size	11
2.6a. Equivalent blackbody temperatures ($^{\circ}\text{K}$) from channel 8 ($11\text{ }\mu\text{m}$ atmospheric window) of the HIRS instrument . .	15
2.6b. Radiance values ($\text{ergs s}^{-1}/\text{cm}^{-1}$) of reflected solar radiation ($0.69\text{ }\mu\text{m}$) from channel 17 of HIRS	16
2.7. Surface weather maps at (a) 1200 GMT 20 February 1976 (b) 0000 GMT 21 February 1976 (c) 1200 GMT 21 February 1976 and (d) 0000 GMT 22 February 1976	20
2.8. 500 mb charts at (a) 1200 GMT 20 February 1976 (b) 0000 GMT 21 February 1976 (c) 1200 GMT 21 February 1976 and (d) 0000 GMT 22 February 1976	22
2.9. Radar Summaries at (a) 1200 GMT 20 February 1976 (b) 0000 GMT 21 February 1976 (c) 1200 GMT 21 February 1976 and (d) 0000 GMT 22 February 1976	23
2.10. 6-hour precipitation amounts at (a) 1200 GMT 20 February 1976 (b) 0000 GMT 21 February 1976 (c) 1200 GMT 21 February 1976 and (d) 0000 GMT 22 February 1976	25

LIST OF FIGURES (Continued)

<u>Figure</u>		<u>Page</u>
2.11.	GOES - East visual satellite imagery at 1700 GMT 20 February 1976	27
2.12.	GOES - East infrared satellite imagery at 1730 GMT 20 February 1976	29
2.13.	GOES - East infrared satellite imagery at 1630 GMT 21 February 1976	31
2.14.	GOES - East visible satellite imagery at 1700 GMT 21 February 1976	33
3.1.	Rawinsonde stations used in this study	37
3.2.	Nimbus VI orbital passes	39
3.3.	Multiple correlation coefficients array	45
4.1a.	Temperature ($^{\circ}$ K) comparisons of the cloud and precipitation cases for conventional and SCAMS data between T_{SFC} and T_{B1}	51
4.1b.	Temperature ($^{\circ}$ K) comparisons of the cloud and precipitation cases for conventional and SCAMS data between T_{SFC} and T_{B2}	52
4.1c.	Temperature ($^{\circ}$ K) comparisons of the cloud and precipitation cases for conventional and SCAMS data between T_{500} and T_{500S}	53
4.2a.	Temperature ($^{\circ}$ K) comparisons of clear, snow and rain cases for conventional and SCAMS data between T_{SFC} and T_{B1}	56
4.2b.	Temperature ($^{\circ}$ K) comparisons of clear, snow and rain cases for conventional and SCAMS data between T_{SFC} and T_{B2}	57
4.2c.	Temperature ($^{\circ}$ K) comparisons of clear, snow and rain cases for conventional and SCAMS data between T_{500} and T_{500S}	58
4.3.	Temperature ($^{\circ}$ K) comparisons of the rain cases for conventional and SCAMS data between (a) T_{SFC} , T_{B1} (b) T_{SFC} , T_{B2} and (c) T_{500} , T_{500S}	60

LIST OF FIGURES (Continued)

<u>Figure</u>		<u>Page</u>
4.4.	Total vertical motions for the 900, 700 and 500 mb levels at 1200 GMT 21 February 1976	61
4.5.	Rawinsonde soundings for (a) 72349, UMN-Monett, Mo. (b) 72327, BNA-Nashville, Tn. at 1200 GMT 21 February 1976 and (c) 72229 CKL-Centerville, Al. at 1200 GMT 22 February 1976	62
4.6.	Average microwave brightness temperature ($^{\circ}\text{K}$) from the horizontally and vertically polarized components of ESMR	84
4.7.	Linear polarization expressed as a percentage and defined in Eq. 2.3 for microwave brightness temperature of ESMR	86
4.8.	Percentage polarization of ESMR microwave brightness temperature plotted with respect to ESMR average brightness temperature and conventional surface temperature for 20 February 1976	88
4.9.	Radiance values ($\text{ergs s}^{-1}/\text{cm}^{-1}$) from channel 17 of HIRS plotted with respect to infrared temperature from HIRS and average brightness temperature from ESMR for 20 February 1976	89

LIST OF TABLES

<u>Table</u>	<u>Page</u>
2.1. Characteristics of SCAMS Channels	6
2.2. Functions of the HIRS Channels	14
2.3. Parameters derived from conventional meteorological data that were compared with Nimbus VI measurements	18
3.1. List of parameters and the symbols used to identify each in the linear and multiple correlation coefficients	42
4.1. Linear correlation coefficients for all cases for SCAMS brightness temperatures for two data groups . .	47
4.2. Linear correlation coefficients between SCAMS brightness temperatures and surface temperatures from rawinsonde observations	48
4.3. Linear correlation coefficients of 500 mb temperatures obtained from rawinsonde observations and SCAMS temperature retrievals	49
4.4. Linear correlation coefficients for Group 1 data set for clear and overcast conditions and cases with and without precipitation	50
4.5. Linear correlation coefficients for Group 2 data set for clear and overcast conditions and cases with and without precipitation	54
4.6. Linear correlation coefficients for Group 1 data set for clear cases with relative humidities less than 25% and non-precipitating overcast conditions for low, middle, and high clouds	64
4.7. Linear correlation coefficients for Group 2 data set for clear cases with relative humidities less than 25% and non-precipitating overcast conditions for low, middle, and high clouds	65

LIST OF TABLES (Continued)

<u>Table</u>		<u>Page</u>
4.8.	Multiple correlation coefficients for Group 1 between SCAMS brightness temperatures from channel 1 with surface temperature measurements from rawinsonde measurements and channel 2 data	67
4.9.	Linear correlation coefficients between channel 1 brightness temperatures and rawinsonde surface temperatures for different terrain heights from Group 1 data	68
4.10.	Linear and multiple correlation coefficients of SCAMS measurements and conventional observations to show terrain effects for Group 1 data set	70
4.11.	Average brightness temperatures ($^{\circ}$ K) from SCAMS data for observation times near local midnight (05 to 08 GMT) and local noon (15 to 19 GMT) over the North American Continent for a) clear cases only and b) precipitation cases	72
4.12.	Linear correlation coefficients between ESMR vertically and horizontally polarized brightness temperature and SCAMS brightness temperature from channel 1 and 2 from Group 2 data	74
4.13.	Linear correlation coefficients for Group 2 for ESMR, SCAMS, and conventional data under different cloud conditions	76
4.14.	Linear correlation coefficients for ESMR brightness temperatures and percentage polarization with conventional meteorological data and SCAMS measurements for precipitating and non-precipitating cases	78
4.15.	Linear correlation coefficients for Group 2 ESMR and conventional meteorological data for different terrain heights	80
4.16.	Linear correlation coefficients of rawinsonde surface and 500 mb temperatures, compared to HIRS equivalent blackbody temperature and reflected solar radiation channel data	82

LIST OF TABLES (Continued)

<u>Table</u>		<u>Page</u>
4.17.	Linear correlation coefficients of SCAMS surface temperatures and HIRS reflectance measurements clear and overcast conditions and cases with and without precipitation	82

ACKNOWLEDGEMENTS

I wish to extend my sincere thanks to Dr. Elford G. Astling for the guidance, assistance and support he gave me during the preparation of this thesis.

I am also grateful to my fellow students who offered their support and assistance during the critical final days of the thesis preparation. Also, I wish to express my appreciation to Deanna Plumhof who expeditiously typed this thesis under time-critical circumstances.

Special thanks to my wife, Ginger, and sons Greggry and Ronald for their encouragement, assistance, patience and understanding during this research.

This research was supported by the Air Force Geophysics Laboratory, Bedford, Massachusetts under Grant F19628-78-C-0130.

CHAPTER I

INTRODUCTION

Research meteorological satellites have provided useful meteorological data during the past two decades. Recent satellite instrumentation has continued to improve with theoretical and technological advancements in multispectral remote sensing of the earth-atmosphere system. Newer research satellites have provided data in the visible, infrared and microwave spectral regions to make it possible to study remote sensing of such meteorological parameters as clouds, precipitation, atmospheric temperature, snow cover, and soil moisture.

In this study data from Nimbus VI meteorological satellite were investigated for a wintertime synoptic case when a mid-latitude cyclone traversed the North American Continent. Many different types of clouds and weather were associated with this cyclone from 19 to 22 February 1976 over the United States and southern Canada where conventional meteorological data were available.

The primary objective was to find if there was correlative information between multispectral measurements from Nimbus VI and conventional meteorological data such as surface and rawinsonde observations. Multispectral measurements from Nimbus VI were compared with surface and rawinsonde meteorological observations. Visible and infrared geostationary satellite imagery was also included to enhance conventional analyses of moisture, cloud and precipitation fields.

In addition, the effects of clouds and precipitation on satellite derived temperature for the surface and mid-tropospheric levels were considered. Various statistical analyses were carried out using up to 19 different conventional and satellite derived meteorological parameters.

CHAPTER II

DATA SOURCES AND SYNOPTIC SITUATION

The data for this study were obtained from a number of sources. These include data from Nimbus VI and GOES meteorological satellites, rawinsonde observations and other conventional meteorological measurements. In addition, results from numerical computations in a previous study of a February, 1976 mid-latitude cyclone by Hall (1979) were used in this investigation. Nimbus VI remote measurements of radiation upwelling at different spectral frequencies were provided in digital form from the National Space Science Data Center (NSSDC) at NASA's Goddard Space Flight Center. The GOES satellite data were obtained from the National Climatic Center and consisted of visible and infrared images from two geostationary satellites that viewed the North American Continent. Other conventional and numerical data were available from the extensive files in the Department of Meteorology at the University of Utah.

Nimbus VI Satellite Data

Nimbus VI was launched on 12 June 1975 in a sun-synchronous polar orbit at an altitude of 1100 km. The satellite provided nearly complete global data coverage with approximately three successive orbital passes over the North American Continent per day, with ascending passes near local noon and descending passes near local midnight (Nimbus VI User's Guide, 1975). The orbital period was nearly

107 minutes and the longitude separation between successive orbits over the United States was approximately 15° at 40° N Latitude.

The multispectral radiance measurements from the Nimbus VI research satellite included solar reflection and thermal emission from several wavelength bands in the infrared and microwave regions. These measurements were obtained from the SCAMS (Scanning Microwave Spectrometer), ESMR (Electrically Scanning Microwave Radiometer), and HIRS (High Resolution Infrared Radiation Sounder) experiments on board Nimbus VI. The radiance measurements were used by NASA to derive equivalent blackbody temperatures for infrared wavelengths and brightness temperatures for the microwave channels according to techniques described in the Nimbus VI Users Guide (1975). Atmospheric temperature soundings were also derived by NASA from the data at microwave frequencies and were available on the NASA magnetic data tapes for use in this study.

Scanning Microwave Spectrometer Experiment (SCAMS)

The SCAMS instrument was a five channel radiometer that measured emitted thermal radiation in the microwave region between 0.54 to 1.35 cm. At these wavelengths, the microwave instrument provided measurements over land areas that were sensitive to a different degree to the terrestrial surface, clouds, precipitation, water vapor, and the atmospheric temperature profile. The microwave brightness temperature $[T_B(\nu)]$ derived from the satellite measurements can be approximated by

$$T_B(\nu) = \epsilon T_s e^{-\tau_\nu} + \int_0^\infty T(h)w(h,\nu)dh \quad (2.1)$$

where ϵ is the emissivity, T_s is surface temperature, $e^{-\tau_v}$ is atmospheric transmissivity, $T(h)$ is the atmospheric temperature at level h , and $w(h,v)$ is a weighting function. The first term on the right in Eq. 2.1 represents the component contributed by the surface while the second term primarily is the atmospheric component for the oxygen bands. If the value of ϵ is substantially less than 1.0, then a third term in Eq. 2.1 is needed which is proportional to surface reflectivity $(1-\epsilon)$.

The characteristics about each of the five microwave channels of SCAMS are summarized in Table 2.1. The two channels at 1.350 and 0.948 cm wavelengths were sensitive to atmospheric water in both vapor and liquid form and modulated microwave radiation that was emitted from the earth's surface. Generally for these two channels, the first term on the right-hand side of Eq. 2.1 was the primary contributor to brightness temperature. The other three channels, for wavelengths between 0.568 and 0.541 cm, were primarily sensitive to thermal emission by oxygen and were nearly unaffected by liquid water except in very unusual cases as noted by Hayden (1979). Brightness temperatures derived from these three channels were dominated by the second term on the right-hand side of Eq. 2.1 and were used to obtain atmospheric temperature profiles (Staelin, et al, 1975).

Vertical profiles of the weighting function $w(h,v)$ in Eq. 2.1 for each of the oxygen channels from SCAMS is shown in Fig. 2.1. These profiles were used by NASA for the temperature retrievals to obtain 1000 and 500 mb temperatures that were used in this study. The weighting functions were dependent on the viewing angle, atmospheric vertical temperature profile, atmospheric water content, and radiation

Table 2.1. Characteristics of SCAMS Channels

Channel	Frequency (GHz)	Wavelength (cm)	Absolute Accuracy ($^{\circ}$ K rms)	Principal Absorbing Constituent	Primary Purpose
1	22.235	1.350	2.0	Water Vapor	Determination of surface emissivity, temperature, and properties of ice types; snow cover and soil moisture.
2	31.650	0.948	2.0	Atmospheric Window	
3	52.850	0.568	2.0	Oxygen	Atmospheric Temperature Profiles (See Fig. 2.1)
4	53.850	0.557	2.0	Oxygen	
5	55.450	0.541	2.0	Oxygen	

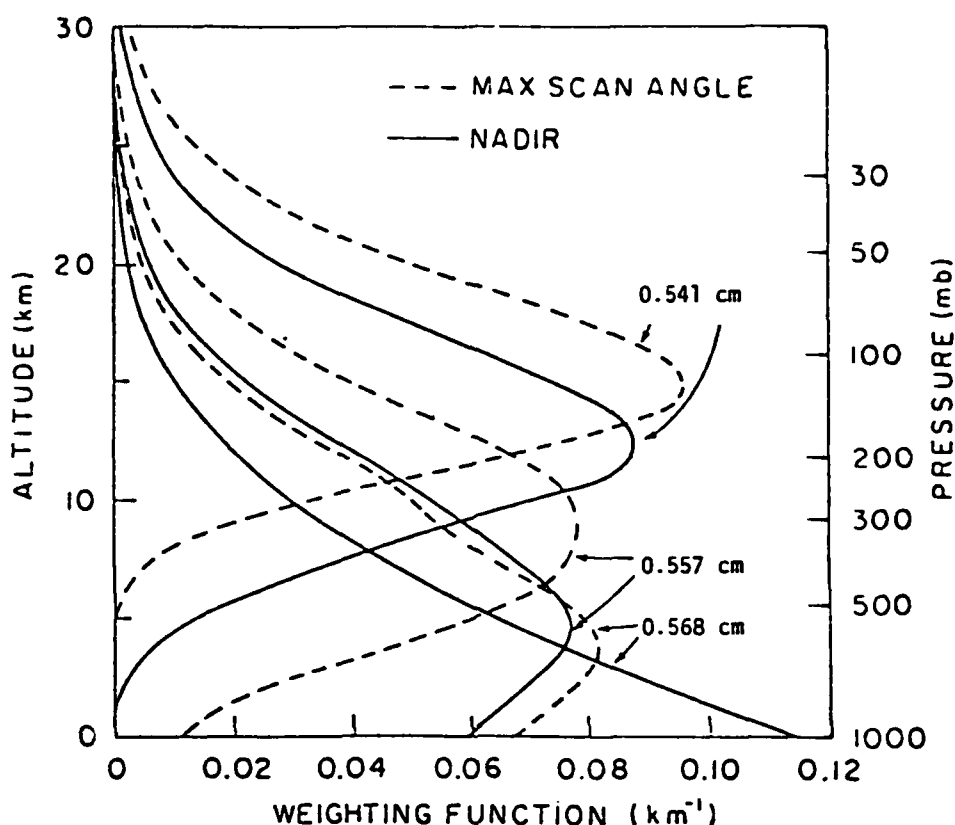


Figure 2.1. SCAMS Weighting Function according to Nimbus VI Users Guide (1975).

properties of the underlying surface. It can be seen from Fig. 2.1 that the weighting functions reached a peak value at lower levels at nadir than at maximum viewing angles. At the 0.568 cm wavelength (channel 3) the weighting function was at maximum in the lower troposphere, while at successively shorter wavelengths within these oxygen bands, the weighting function peaked at progressively higher atmospheric levels, so that the 0.541 cm wavelength band was most sensitive in the lower stratosphere.

It should be noted that these vertical profiles assumed the

underlying surface was seawater. More recent studies by Grody and Pellegrino (1977) have shown that peak values of the weighting functions in this spectral region occur at somewhat lower levels over land areas. This may be attributed to emissivity differences in the microwave region where values over land approach unity as compared to a water surface where emissivities may be as low as 0.5.

The SCAMS instrument viewed the earth-atmosphere along a scan path that was swept out perpendicular to the satellite orbital track. Thirteen data samples were obtained per scan line with a spatial resolution of approximately 145 km near nadir to 330 km at the scan limit where the angle of view was 43° . A sample distribution of scan point locations is shown in Fig. 2.2 for orbit 3411 over the western United States on 21 February 1976. The dots in Fig. 2.2 represent the position of the center of each scan beam which viewed a nearly circular area that overlapped with adjacent scan points and provided continuous data coverage along the satellite orbital track.

Electrically Scanning Microwave Radiometer Experiment (ESMR)

The ESMR instrument was a single channel radiometer that measured thermal microwave upwelling from the earth's surface and atmosphere within a narrow spectral region centered at 0.81 cm. Microwave brightness temperature data were obtained from this instrument and were used to map liquid water content of clouds over oceanic regions as well as variation of sea ice cover, snow cover on ice and characteristics of land surfaces such as soil moisture.

The ESMR instrument measured both the horizontally and vertically polarization components in the 0.81 cm wavelength region.

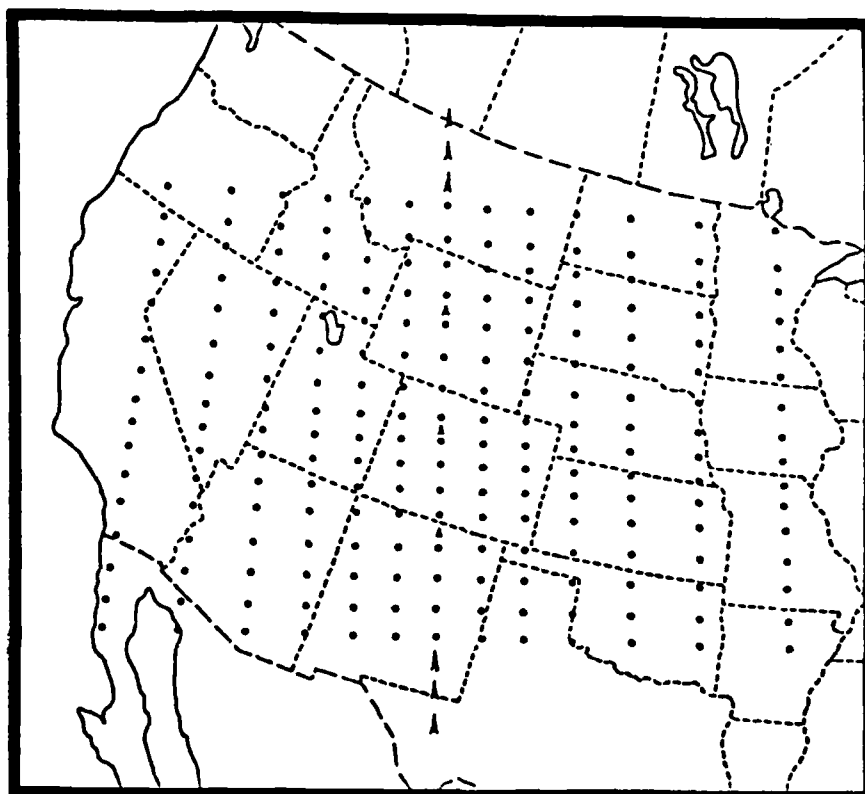


Figure 2.2. SCAMS scan point locations at 1815 GMT 21 February 1976.

Measurements of the horizontal and vertical components provided polarization information which facilitated the quantitative interpretation of the radiometric measurements. In particular, the reflectivity of sea ice or dry land is essentially unpolarized while the reflectivity of a water surface is highly polarized. Therefore, the amount of polarization was used to investigate the identification of dry soil versus wet soil and snow-covered versus snow-free surfaces.

The ESMR vertical and horizontal brightness temperatures were

designated by T_B^v and T_B^h , respectively. The average brightness temperature was defined as:

$$T_{AVG} = (T_B^v + T_B^h)/2 \quad (2.2)$$

and degree of linear polarization as:

$$P(\%) = \frac{T_B^v - T_B^h}{T_B^v + T_B^h} \times 100\% \quad (2.3)$$

The antenna beam of the ESMR scanned ahead of the space craft along a conical surface with a constant angle 45° with respect to the antenna axis. The beam scanned $\pm 35^\circ$ with respect to azimuth about the forward direction in 71 steps such that the first beam position was at an azimuth angle of 35° to the right of the space craft, the 36th beam position viewed straight ahead, and 71st beam position viewed 35° to the left. Consequently, this scan geometry maintained a viewing angle that varied by less than 1 degree and minimized brightness temperature variations due to this effect.

Figure 2.3 shows the scan point locations of ESMR data for a subsection of an orbital swath over Utah. These data points were from the same orbit as the SCAMS information shown in Fig. 2.2; however, it can be seen that the ESMR instrument had a higher resolution than SCAMS and ranged from 25 km near nadir to 125 km at the end of the scan sweep.

In order to reduce the differences in spatial resolution, so that ESMR and SCAMS data could be readily compared, a Cressman (1959) type of objective analysis scheme was applied to the ESMR data. More

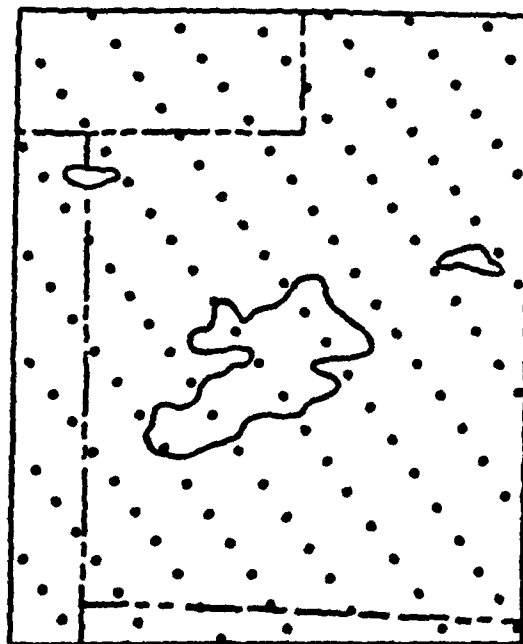


Figure 2.3. ESMR scan point locations for a subsection of Nimbus VI orbital pass over northern Utah on 21 February 1976.

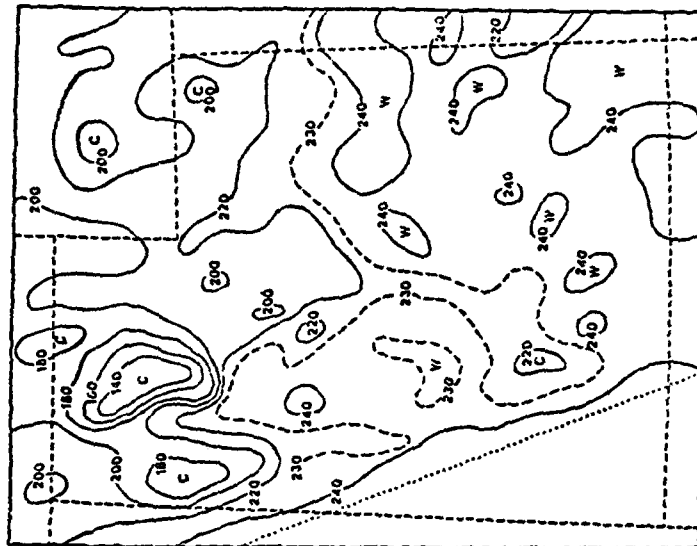


Figure 2.4. Subjective analysis of average brightness temperatures ($^{\circ}\text{K}$) obtained from ESMR at 1815 GMT 21 February 1976.

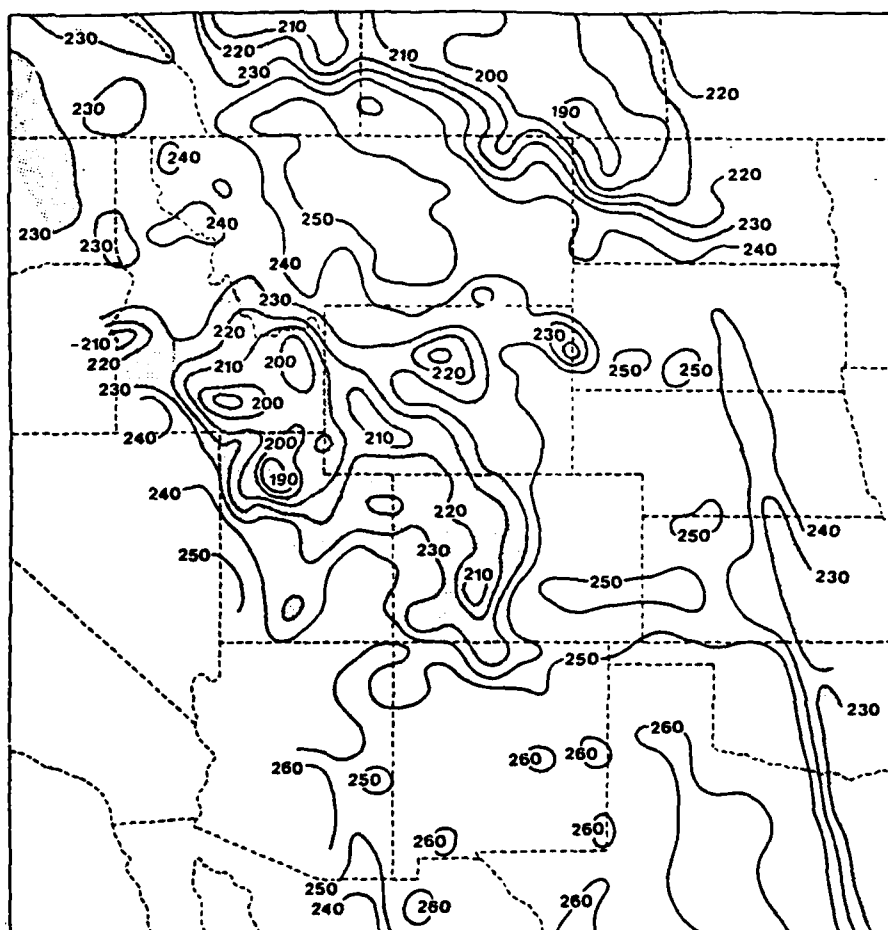


Figure 2.5. Objectively analyzed brightness temperatures ($^{\circ}\text{K}$) from ESMR for a $1/2^{\circ}$ latitude-longitude grid size. These data were obtained from orbit 3411 of Nimbus VI on 21 February 1976 at approximately 1815 GMT.

detail about the application of this scheme to Nimbus VI data is discussed by Astling and Liou (1979). After experimentation with different grid sizes, a radius of influence of $1/2^\circ$ latitude was chosen and average brightness temperatures and percentage of polarization were mapped onto a $1/2^\circ$ latitude-longitude grid array. Subjective analyses from individual scan point data with an objective analysis are shown in Figs. 2.4 and 2.5, respectively.

High Resolution Infrared Radiation Sounder Experiment (HIRS)

The Nimbus VI HIRS was an instrument with the capability of remote sensing the earth's atmosphere to obtain vertical temperature profiles under all but extensive cloud conditions. The instrument obtained simultaneous measurements in 17 discrete spectral intervals within the visible and infrared regions. Only two of the instruments 17 spectral bands were relevant to this study and were used to supplement other meteorological information and to analyze microwave data from the SCAMS and ESMR instruments. One band (channel 17) measured reflected sunlight at $0.69 \mu\text{m}$ and was limited to daytime orbits to quantitatively detect clouds. The other spectral band (channel 8) measured radiances in the $11.0 \mu\text{m}$ infrared window to permit quantitative estimates of cloud top heights. Information about these two channels on HIRS are listed in Table 2.2

The scan geometry of the HIRS instrument on Nimbus VI was similar to SCAMS. The instrument scanned along a direction perpendicular to the satellite subpoint track with 42 elements along each scan line. The resolution was 25 km at nadir and was similar to ESMR except for

Table 2.2. Functions of the HIRS Channels

Channel Number	Channel Central Wave-number	Central Wavelength (μm)	Principal Absorbing Constituents	Level of Peak Energy Contribution	Purpose of the Radiance Observation
8	900	11.0	Window	Surface	Surface Temperature and cloud detection.
17	14,443	0.69	Window	Cloud	Cloud Detection. Used during the day to identify clear and cloudy fields of view.

the angle of view. Calibration of HIRS occurred at every 20-th scan line and no measurements were obtained for those points. Consequently, linear data interpolations were made from the scan elements adjacent to the calibration swath in order to provide a continuous field of HIRS data.

An objective analysis of HIRS data was carried out with the same technique that was applied to the ESMR data. A $1/2^\circ$ latitude-longitude grid size array was used to objectively map the HIRS data on to the same scale as the ESMR data so that comparisons could be made between the different instruments. Figures 2.6a and 2.6b show objective analyses of equivalent black body temperatures ($^\circ\text{K}$) derived from channel 8 measurements and radiance values ($\text{ergs s}^{-1} \text{cm}^{-2} \text{sr}^{-1}/\text{cm}^{-1}$) from channel 17 of the HIRS instrument over the central United States on 20 February 1976 (Peyrefitte and Astling, 1980). Results in the comparison of HIRS data with microwave measurements will be discussed in Chapter IV.

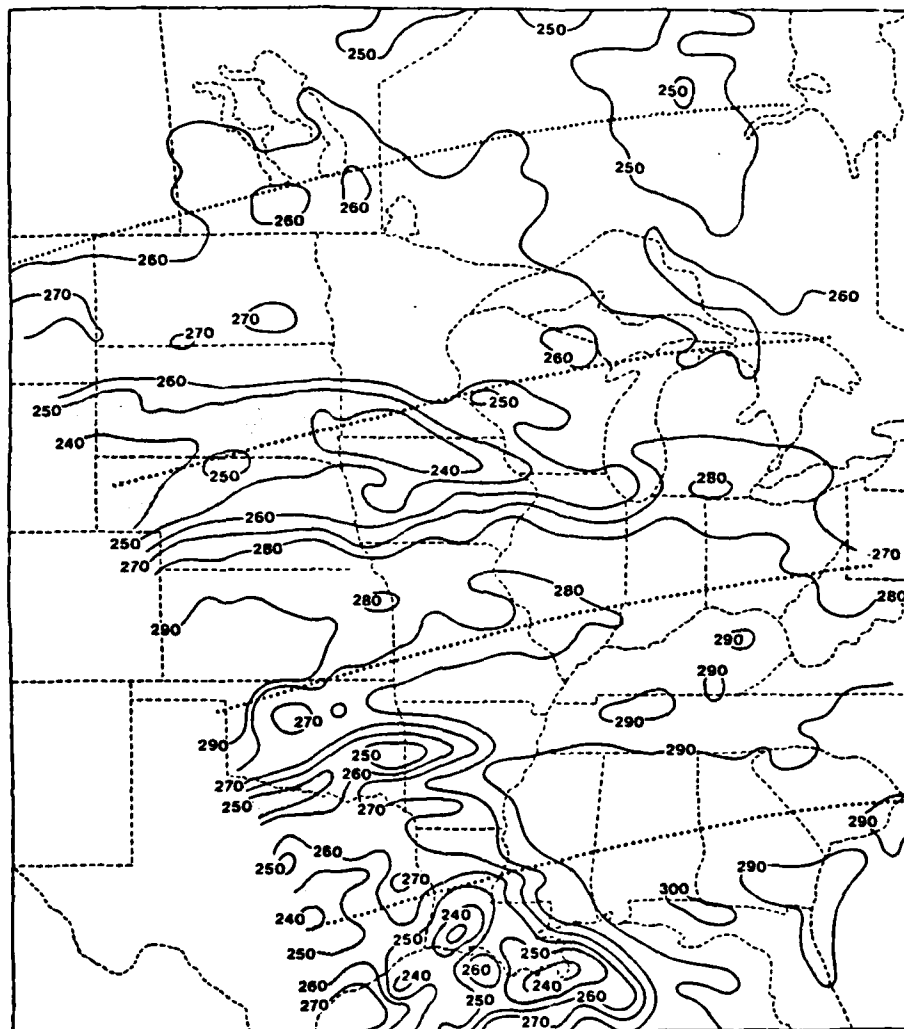


Figure 2.6a. Equivalent blackbody temperatures ($^{\circ}\text{K}$) from channel 8 ($11\text{ }\mu\text{m}$ atmospheric window) of the HIRS instrument. These data were obtained from orbit 3397 of Nimbus VI on 20 February 1976 at approximately 1710 GMT. Dotted lines represent scan lines when HIRS was calibrated.

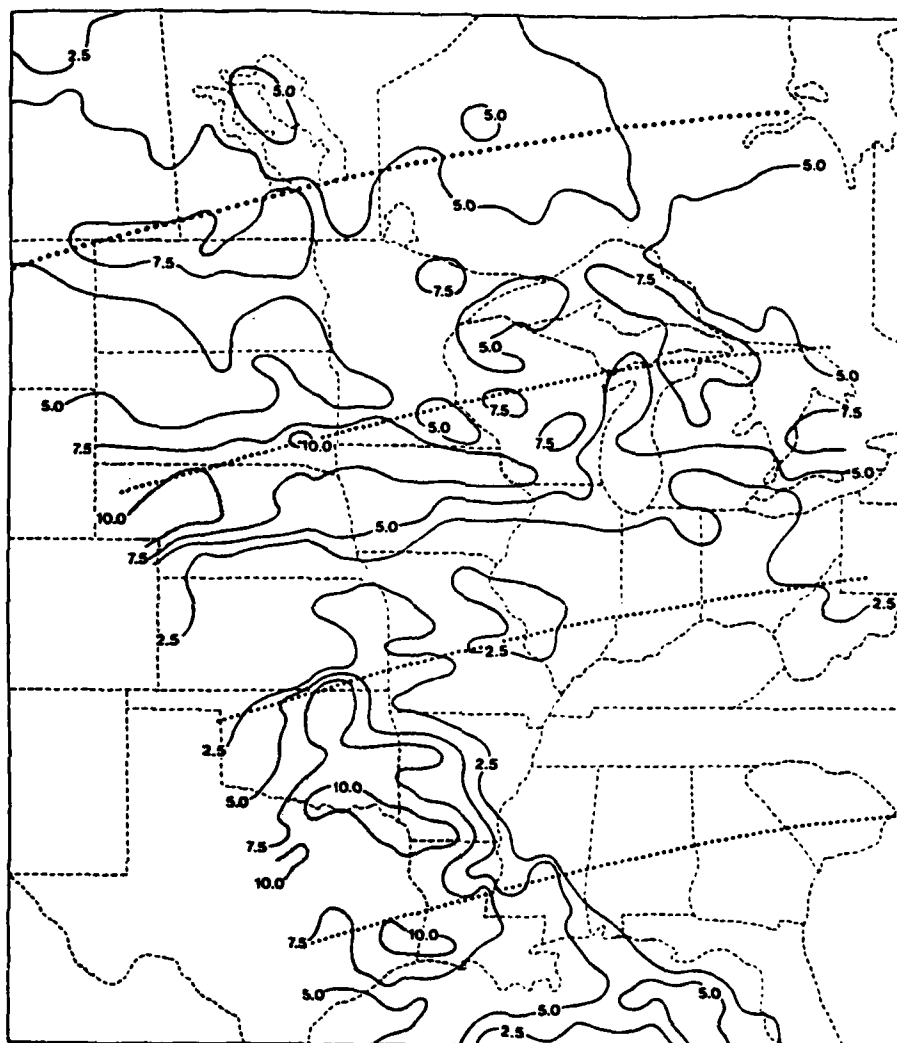


Figure 2.6b. Radiance values ($\text{ergs s}^{-1}/\text{cm}^{-1}$) of reflected solar radiation ($0.69 \mu\text{m}$) from channel 17 of HIRS. These data were obtained from orbit 3397 of Nimbus VI on 20 February 1976 at 1710 GMT.

Conventional Meteorological Observations

Surface and upper air parameters of temperature, clouds, moisture, and visibility restrictions were obtained from a number of sources. Rawinsonde data were used to provide information for surface and 500 mb temperatures and relative humidities. These were available at eight successive 12-hour intervals beginning at 0000 GMT 19 February 1976 and were linearly interpolated to the nearest Nimbus VI orbital pass. Sea level pressure maps, weather depiction charts, national radar summaries, and hourly aviation surface observations for the synoptic times nearest to the Nimbus VI measurements were used to provide data for the other meteorological parameters. These are summarized in Table 2.3.

GOES Visible and Infrared Imagery

Two geostationary satellites provided an additional data source that were helpful in supplementing the conventional meteorological analysis of moisture and cloud fields. These data were available at 30-minute time intervals and made it possible to obtain satellite cloud imagery very close to the time of Nimbus VI orbital passes. The GOES satellites were equipped with a visible and infrared spin scan radiometer with a resolution of 1.2 km for the visible channel and 12 km for the infrared channel. Both day and night coverage were available from the infrared imagery which detected thermal radiation in the 10.5 to 12.5 μm region (Corbell, et al., 1977).

Synoptic Situation

The predominant synoptic system that provided several different types of clouds and weather to investigate in this study was a mid-

Table 2.3. Parameters derived from conventional meteorological data that were compared with Nimbus VI measurements.

Temperature	Cloud Type and Amount	Visibility Restrictions	Moisture and Precipitation
Sea Level 500 mb	low middle overcast 0 - clear 1 - scattered 2 - broken 3 - overcast 4 - obscured	0 - unrestricted 1 - haze 2 - smoke 3 - fog 4 - dust 5 - rain 6 - snow 7 - ice crystals 8 - thunderstorm	relative humidity at surface relative humidity at 500 mb light precipitation moderate precipitation heavy precipitation non-convective convective rain snow

latitude cyclone. This system moved eastward across the United States and southern Canada from 19 to 22 February 1976. The storm entered the Pacific coast as a weak surface low which began to develop over the Great Basin early on 19 February. By 0000 GMT on 20 February, the surface low moved to the Utah-Colorado border as a low-level trough formed downstream on the lee of the Rockies in northeastern Colorado while the upper level trough was still somewhat to the west over northeastern Nevada. This feature is often found with cyclones that move across the intermountain region of the western United States. Initially the system was relatively dry with precipitation confined to a limited area over northern Colorado and southern Wyoming.

The Surface Low

By 1200 GMT 20 February, the surface cyclone merged with the lee side trough to form a single low pressure center in southeastern Colorado as shown in Fig. 2.7a.

The surface map at 0000 GMT 21 February (Fig. 2.7b) showed the surface low had moved into central Kansas. The low pressure center had not deepened further by this time; however, significant weather developed with this system as the low entered the plains region. The area of strong pressure gradients west of the surface low 12 hours earlier, underwent noticeable strengthening and extended to the north of the system. A warm front stretched east from the low center to Kansas, southeast into Mississippi and across the Gulf of Mexico to the Florida Peninsula. A cold front reached southeastward through the Big Bend area of Texas and southwest to Baja California. By 1200 GMT 21 February (Fig. 2.7c) the surface low had moved into eastern Kansas. The

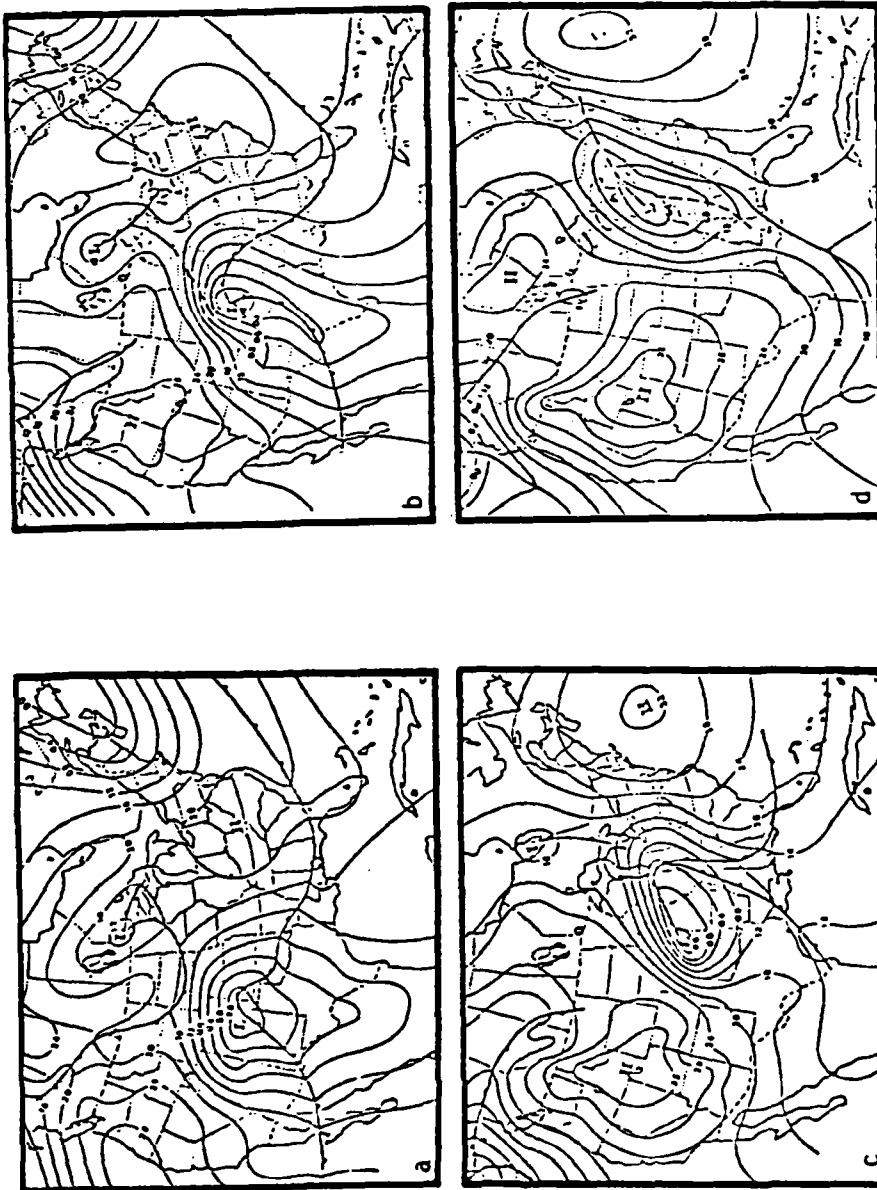


Figure 2.7. Surface weather maps at (a) 1200 GMT 20 February 1976 (b) 0000 GMT 21 February 1976 (c) 1200 GMT 21 February 1976 and (d) 0000 GMT 22 February 1976.

cold front had moved rapidly eastward into northern Indiana and formed a warm front type occlusion that extended back to the cyclone center in eastern Kansas.

The 0000 GMT 22 February map time (Fig. 2.7d) depicted the cyclone over Kansas and it had filled by 4 mb from the previous 12 hours, while a second cyclone formed over Indiana. The surface pressure gradient weakened considerably around the entire storm where the lowest pressure was only 1004 mb. The system continued to weaken and by 0000 GMT 23 February the surface low moved off the east coast of Maine.

The 500 mb Level

The 500 mb trough at 1200 GMT 20 February (Fig. 2.8a) was associated with cold air advection and deepened over western Colorado. By 0000 GMT 21 February (Fig. 2.8b) the trough had progressed eastward into southeastern Colorado. A closed contour appeared at the 500 mb level at the 1200 GMT 21 February (Fig. 2.8c) map time with cold air advection continuing over the New Mexico and west Texas region. The closed contour opened by 0000 GMT 22 February (Fig. 2.8d) and a cold pocket formed over eastern New Mexico and northwest Texas. As the 500 mb trough began to fill, the cold air advection diminished. The 500 mb trough continued to weaken as it followed the surface low into the Atlantic.

The Radar Summaries

Small areas of precipitation echoes were depicted over the northern Colorado region and the Minnesota-Iowa border region by the 1200 GMT 20 February (Fig. 2.9a). The systems' rapid development was

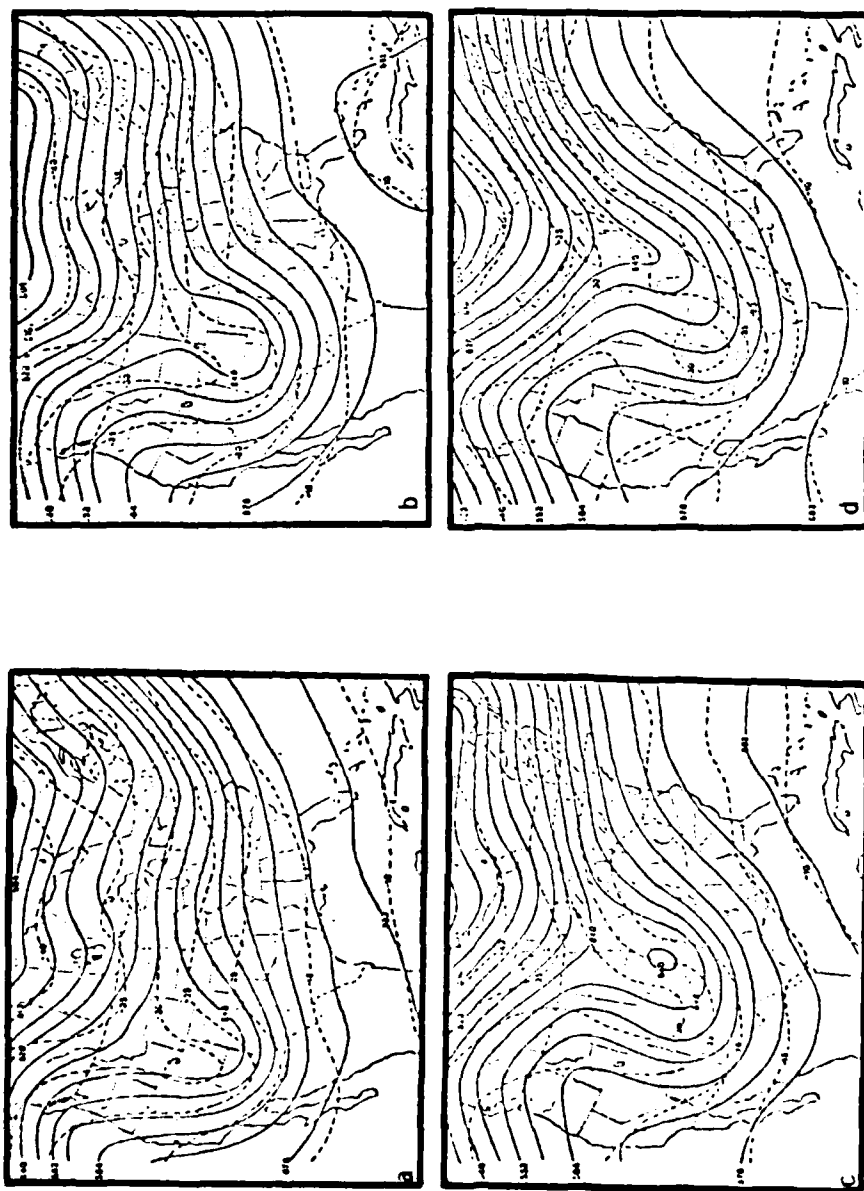


Figure 2.8. 500 mb charts at (a) 1200 GMT 20 February 1976 (b) 0000 GMT 21 February 1976 (c) 1200 GMT 21 February 1976 and (d) 0000 GMT 22 February 1976.

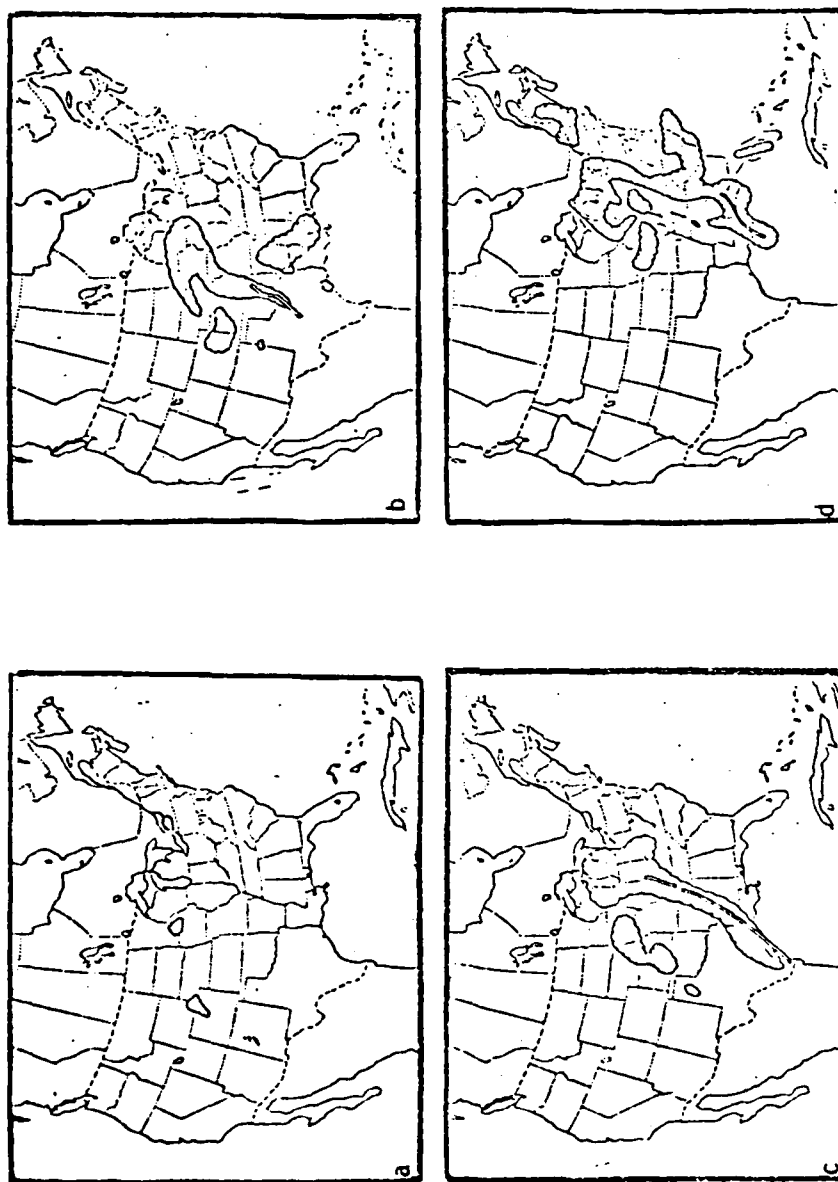


Figure 2.9. Radar Summaries at (a) 1200 GMT 20 February 1976 (b) 0000 GMT
21 February 1976 (c) 1200 GMT 21 February 1976 and (d) 0000 GMT
22 February 1976.

apparent in Fig. 2.9b where a line of thunderstorms had formed in Oklahoma and northern Texas and convective activity ranged to the Great Lakes region. In the following 12 hours, intensification of the convectivity continued and severe weather developed. Fig. 2.9c illustrates the precipitation from the Great Lakes to the southern most tip of Texas with a solid line of severe thunderstorms with tops up to 45,000 feet ahead of the cold front from Indiana to south Texas. By the 0000 GMT 22 February, the Radar Summary (Fig. 2.9d) indicated widespread areas of convective activity over the eastern portion of the United States. A decrease in the intensity of the system was noted where severe thunderstorms were limited to the Gulf of Mexico region. The system progressed eastward with precipitation continuing along the entire United States east coast and severe thunderstorm activity occurred only over Florida as the storm entered the Atlantic.

Six-hour Precipitation Amounts

Precipitation amounts for the previous six hours up to 1200 GMT 20 February are shown in Fig. 2.10a. Relatively light amounts were widespread from the northeastern United States to western Canada and scattered mainly over the western United States region. The 0000 GMT 21 February (Fig. 2.10b) precipitation accumulation amounts ranged from a trace to 0.50 inches in the area from Lake Michigan to the Rocky Mountains. As the system intensified by 1200 GMT 21 February (Fig. 2.10c) heavy soil-soaking rainfall amounts were recorded over the lower Mississippi valley, and widespread precipitation extended from the western Gulf region to the eastern Great Lakes and westward over the Great Plains to the eastern Rockies. Although the severity of the

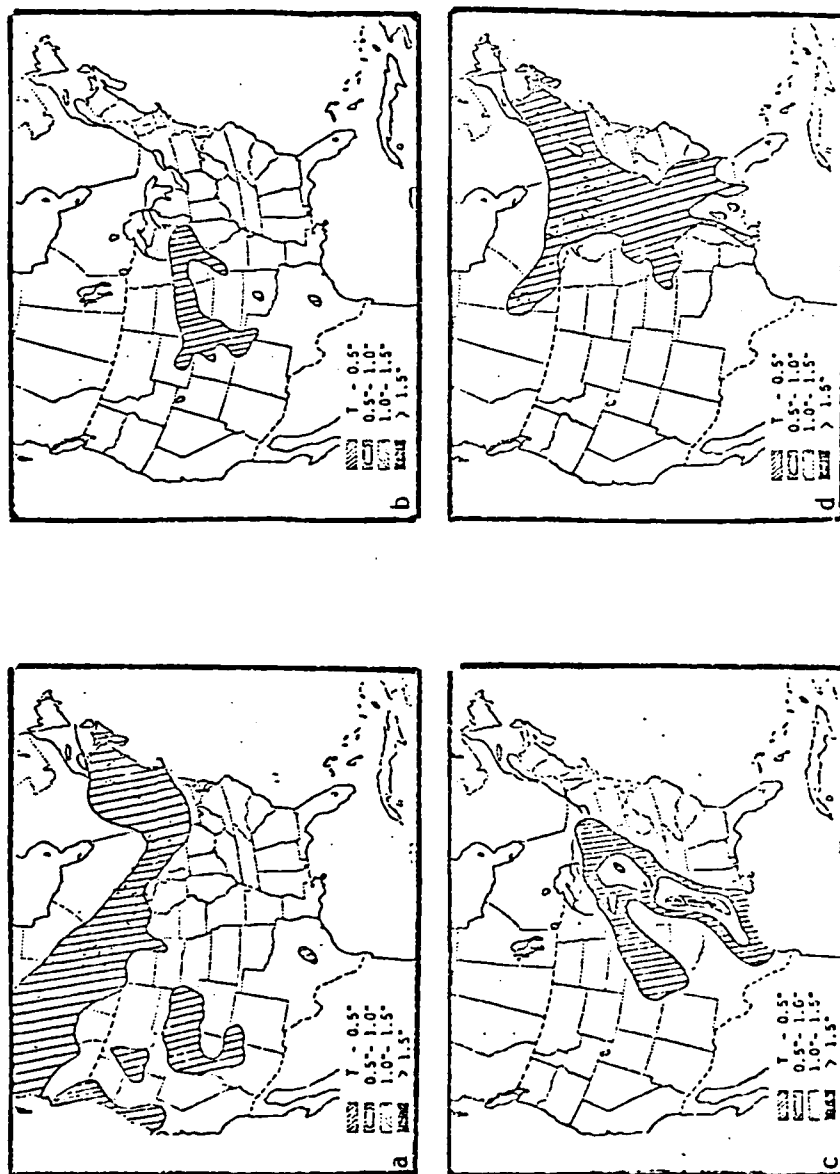


Figure 2.10. 6-hour precipitation amounts at (a) 1200 GMT 20 February 1976 (b) 0000 GMT 21 February 1976 (c) 1200 GMT 21 February 1976 and (d) 0000 GMT 22 February 1976.

system had decreased by 0000 GMT 22 February (Fig. 2.10d), precipitation continued over an ever-increasing area that encompassed most of the United States from the Mississippi Valley eastward to most of the Atlantic coast states and southern Canada. As the system continued eastward on 22 February, precipitation fell on the remaining Atlantic states.

GOES Imagery

Visual and infrared photos in the 1630 to 1730 GMT time frames close to the northbound Nimbus VI satellite passes on 20 and 21 February 1976 showed the system's intensification as the low and associated frontal system progressed into the lee of the Rockies and through the Mississippi Valley to the Great Lakes region. Figures 2.11 and 2.12 show the rapid convective development in the states along the northwestern Gulf region. Clouds and scattered precipitation ranged from the central and northern Rockies to the Great Lakes region. Between the cloudy regions of Texas and Colorado a dry clear sky region was noted. Within this dry region strong winds and blowing dust were reported in the panhandle of Texas. Twelve hours later, Figs. 2.13 and 2.14 show the intensity of the system. The solid line of severe thunderstorms shown in Fig. 2.9c are visibly outlined through the Mississippi Valley to the Great Lakes region. Clouds with imbedded precipitation are also noted over the Great Plains region with the area over the Rockies becoming less moist.

In summary, except in the southwestern desert of the United States, which remained relatively dry, precipitation fell over most regions encompassed in this study during the four-day period. Soil

Figure 2.11. GOES - East visual satellite imagery at 1700 GMT 20 February 1976.



Figure 2.12. GOES - East infrared satellite imagery at 1730 GMT 20 February 1976.

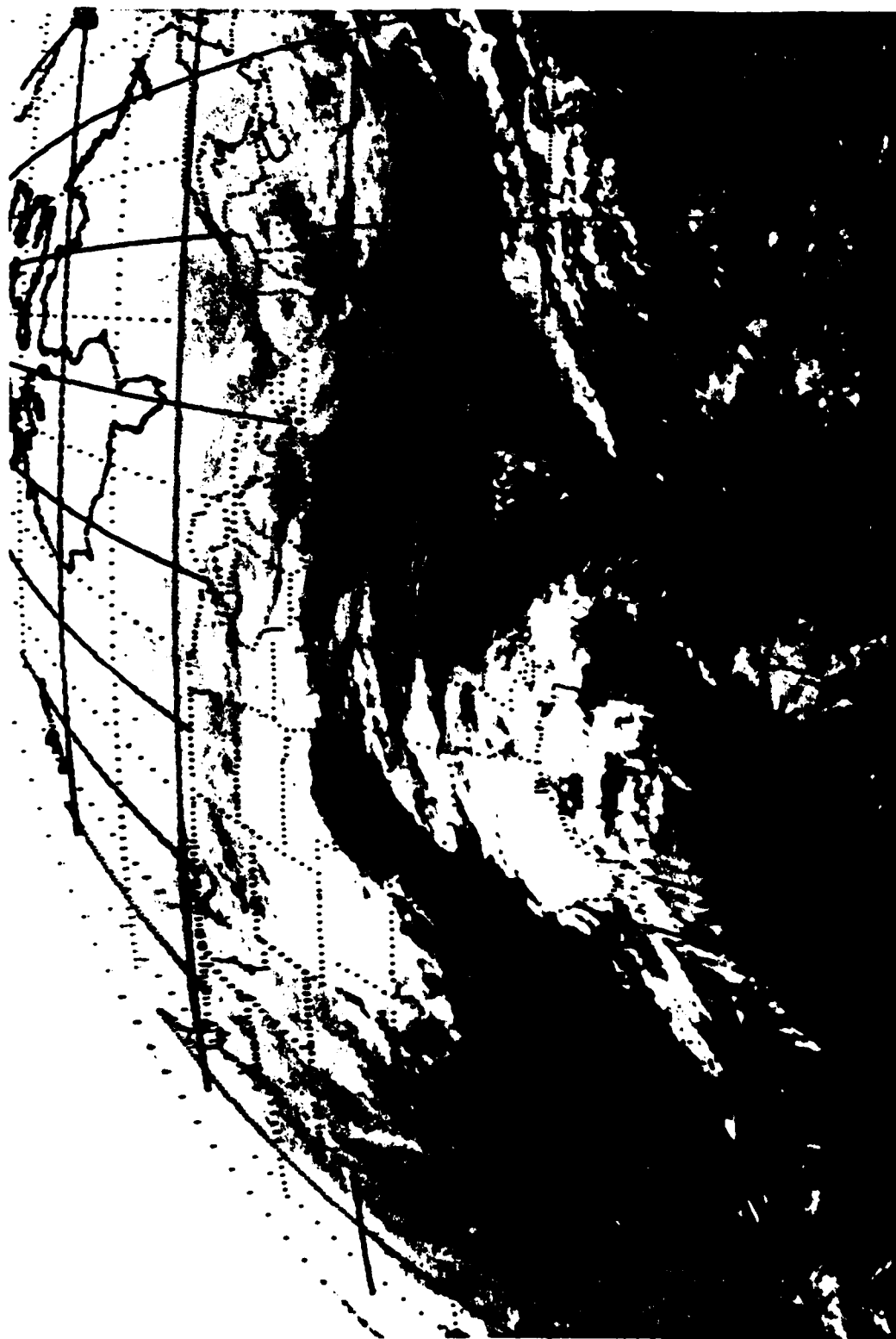


Figure 2.13. GOES - East infrared satellite imagery at 1630 GMT 21 February 1976.

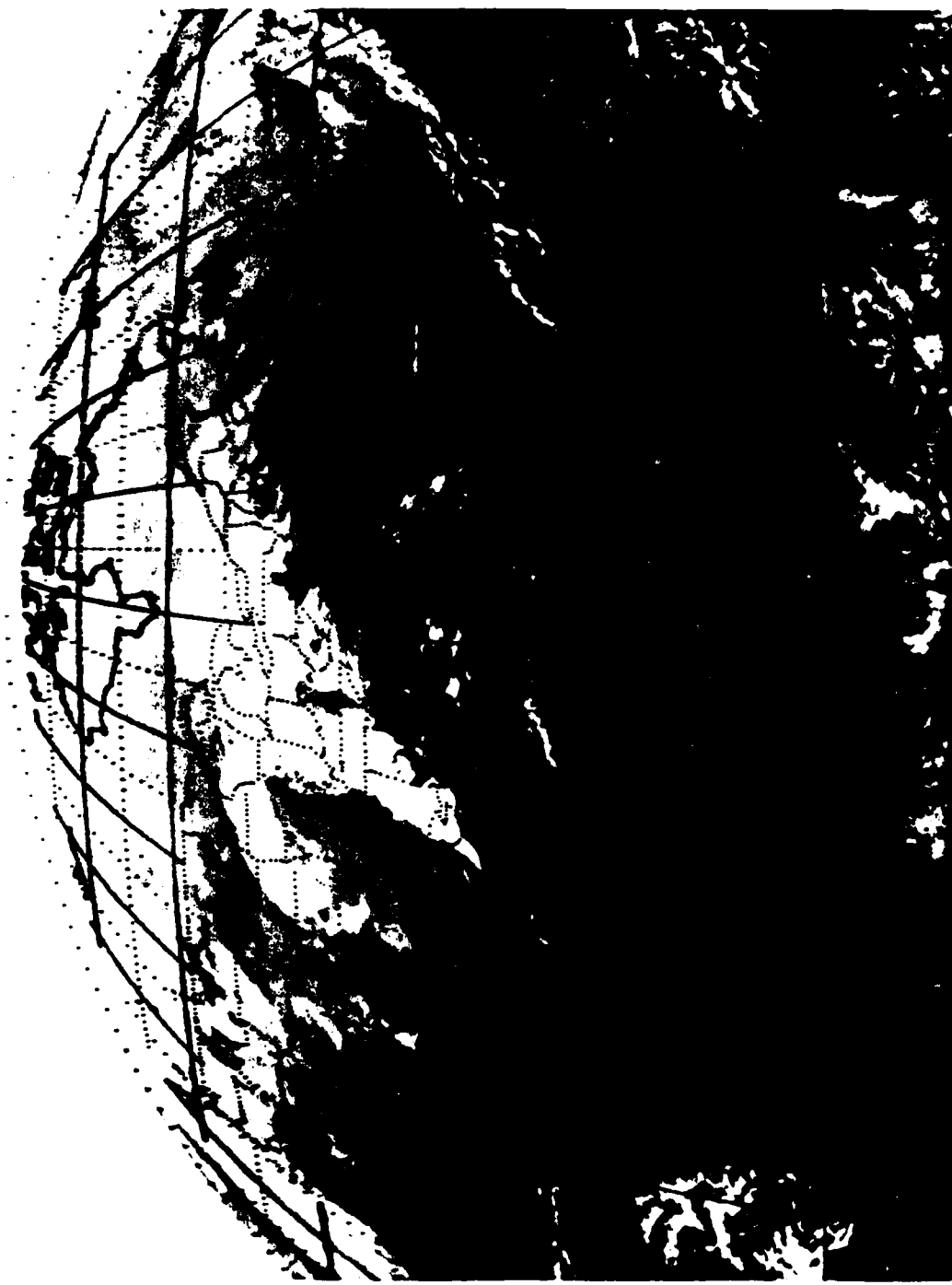
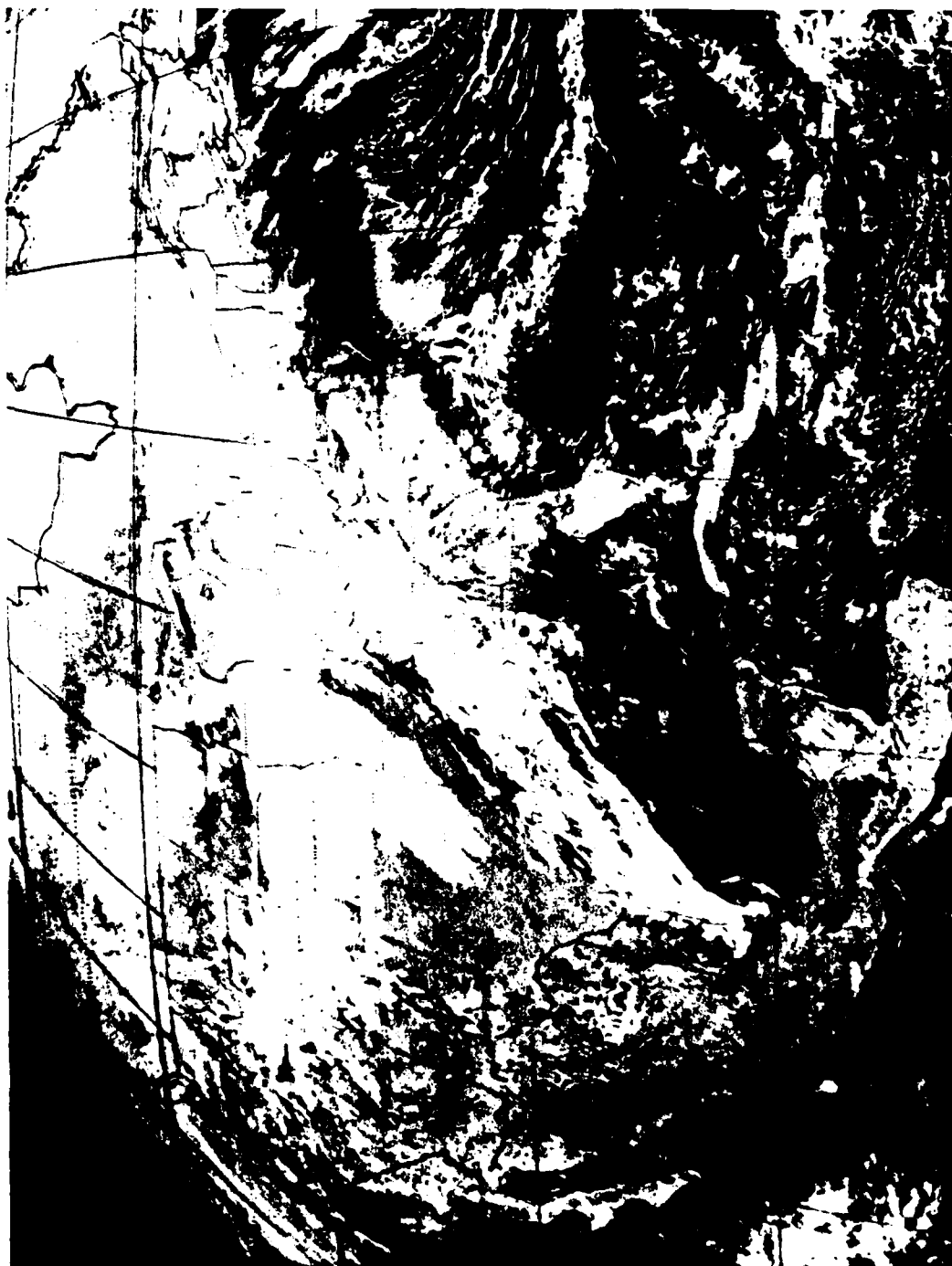


Figure 2.14. GOES - East visible satellite imagery at 1700 GMT 21 February 1976.



moistures varied from dry to saturated and skies ranged from thick overcast to clear and unrestricted conditions. Temperatures at both the surface and 500 mb varied from relatively warm ahead of the surface cold front and 500 mb trough, with cold temperatures behind the front at upper levels. The range of variation of these parameters and its effect on microwave and infrared remote satellite radiometer measurements will be noted in the discussion of results in Chapter IV.

CHAPTER III

ANALYSIS PROCEDURE

The geographical region selected for this study included the continental United States and Canada south of 55°N latitude. There were 45 Rawinsonde stations that provided conventional meteorological data within this region. Locations of these stations are shown in Fig. 3.1. Rawinsonde stations located within approximately a two-degree radius of significantly large bodies of water (sea surfaces and lakes) were excluded from this study because the primary research emphasis here was focused on remote sensing over land areas. Previous studies have shown that there are distinct differences in the microwave characteristics between land and water surfaces due to surface emissivities (Grody, et al, 1977). This was evident in the microwave brightness temperatures in Fig. 2.5 for the Great Salt Lake area.

Data Availability

Conventional data parameters, referenced in Chapter II, were correlated with SCAMS, ESMR and HIRS data. For the four-day period from 19 to 22 February 1976, encompassing the winter cyclone's track across the United States and southern Canada, the maximum number of cases possible was 360 for SCAMS and 90 for ESMR and HIRS data. The variability in the maximum number of cases for the respective radiometers was due to the availability of data from NASA for this time period.

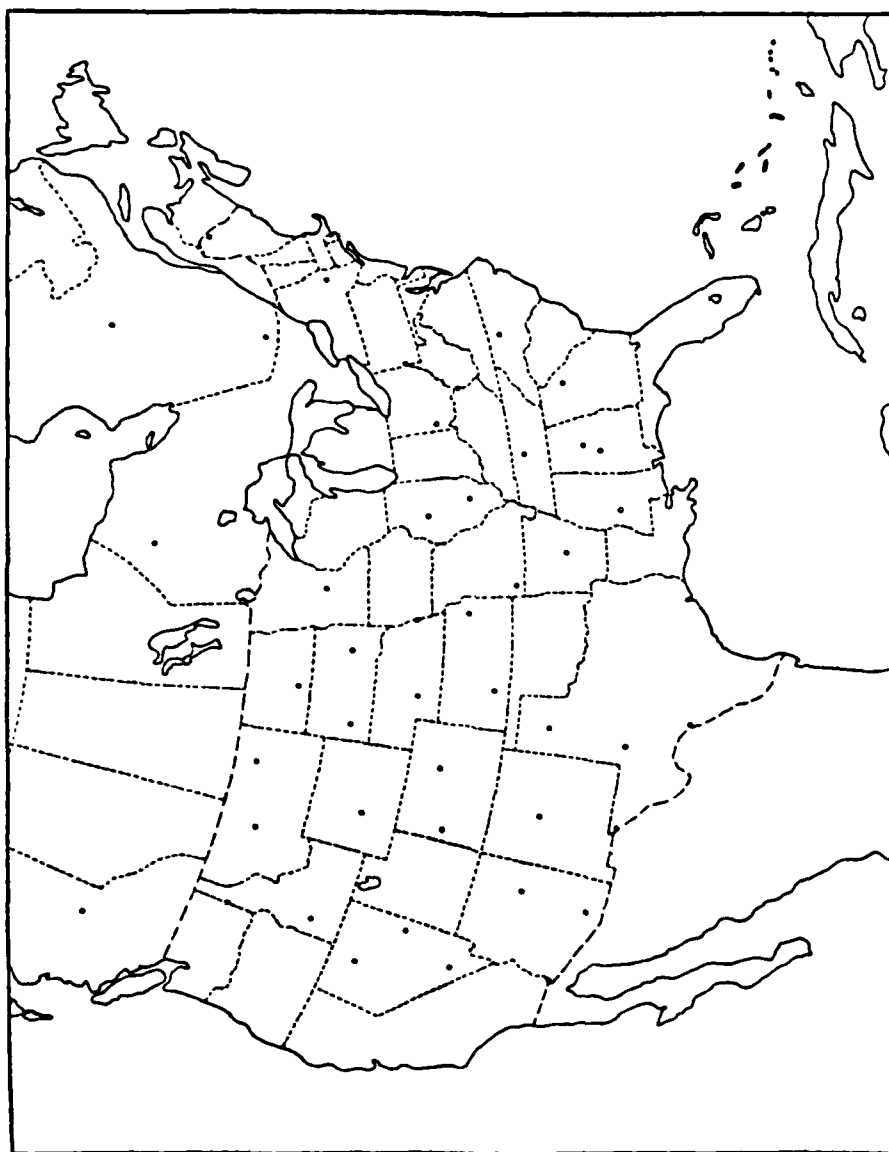


Figure 3.1. Rawinsonde stations used in this study.

This study was conducted by considering data availability in two time groups. One consisted of conventional meteorological observations and SCAMS measurements for eight time periods from 19 to 22 February. A second included conventional data and SCAMS, ESMR and HIRS measurements obtained from the Nimbus VI northbound orbits on 20 and 21 February. Selection of complete data sets for all the required parameters reduced the total number of cases for each time group.

Data from the SCAMS radiometer were available for the entire period selected for this study. Nimbus VI northbound orbital passes over North America occurred between approximately 1500 and 1900 GMT each day, and provided complete regional data coverage near local noon. All southbound passes occurred between approximately 0500 and 0900 GMT each day and corresponded to observation times near local midnight over the United States. The data coverage from SCAMS are shown in Fig. 3.2 for the period of study from 19 to 22 February 1976. Whenever the instruments on Nimbus VI were read out by the ground acquisition station at Rosman, North Carolina, no measurements were obtained by the satellite. Therefore, data gaps were present in several orbits shown in Fig. 3.2.

ESMR and HIRS data were available from NASA for only the northbound daytime orbits on 20 and 21 February. Also, HIRS data for 21 February was limited to only the central and eastern half of the United States and Canada.

A linear interpolation method was used to compare SCAMS, ESMR and HIRS data with rawinsonde and surface observation. Rawinsonde station locations provided the grid coordinate points to which the



Figure 3.2. Nimbus VI orbital passes.



Figure 3.2 (Continued). Nimbus VI orbital passes.

digital scan point data from the three Nimbus VI radiometers were collocated. All of the measurements were divided into two data sets. One consisted of 273 cases where SCAMS measurements were collocated with rawinsonde observations. This data set was divided into various subsets according to different cloud and precipitation categories that were identified in Tables 2.1 and 2.3. This data set will be referred to as Group 1. A second data set included 60 cases with ESMR and 47 cases with HIRS measurements in addition to SCAMS and conventional meteorological measurements. This second data set will be identified as Group 2.

Computation and Presentation of Results

Through a statistical technique of computing linear and multiple correlation coefficients, the two data groups were analyzed independently. The linear correlation computational scheme produced numerical quantities which summarized the relationship between any two variables. Comparisons of correlation coefficients provided a statistical method for relating the dependency of different satellite parameters on such meteorological variable as clouds, precipitation, etc.

Table 3.1 denotes the 19 different parameters for which linear and multiple correlation coefficients were computed. Correlations for Group 1 data included parameters 1 to 13 and Group 2 parameters 1 to 19. Linear correlation coefficients were defined as

$$r(x_i, x_j) = \frac{\sum_{n=1}^N (x_{i_n} - \bar{x}_i)(x_{j_n} - \bar{x}_j)}{[\sum_{n=1}^N (x_{i_n} - \bar{x}_i)^2 \sum_{n=1}^N (x_{j_n} - \bar{x}_j)^2]^{1/2}} \quad (3.1)$$

Table 3.1. List of parameters and the symbols used to identify each in the linear and multiple correlation coefficients.

	Symbol	Description	Data Source
1	T_{B1}	Microwave brightness temperature for surface	Channel 1 SCAMS radiometer
2	T_{B2}	Microwave brightness temperature for near surface	Channel 2 SCAMS radiometer
3	T_{B3}	Microwave brightness temperature for lower troposphere	Channel 3 SCAMS radiometer
4	T_{B4}	Microwave brightness temperature for middle troposphere	Channel 4 SCAMS radiometer
5	T_{B5}	Microwave brightness temperature for lower stratosphere	Channel 5 SCAMS radiometer
6	T_{SFC}	Surface temperature from rawinsonde	Northern hemisphere data tabulations
7	RH_{SFC}	Surface relative humidity from rawinsonde	Northern hemisphere data tabulations
8	RH_{500}	500 mb relative humidity from rawinsonde	Northern hemisphere data tabulations
9	T_{500}	500 mb temperature from rawinsonde	Northern hemisphere data tabulations
10	T_{500S}	Microwave derived 500 mb temperature	SCAMS radiometer

Table 3.1. (Continued)

	Symbol	Description	Data Source
11	T_{1000S}	Microwave derived 1000 mb temperature	SCAMS radiometer
12	CLD	Cloud amount	Surface and weather depiction, radar summary and GOES imagery
13	TER	Microwave derived terrain heights	SCAMS radiometer
14	T_B^h	Horizontally polarized brightness temperature	ESMR radiometer
15	T_B^v	Vertically polarized brightness temperature	ESMR radiometer
16	T_{IR}	Infrared temperature	Channel 8 HIRS radiometer
17	REFL	Reflectance measurement	Channel 17 HIRS radiometer
18	T_{AVG}	T_B^h and T_B^v averaged $(T_B^h + T_B^v)/2$	ESMR - Channels T_B^h and T_B^v
19	P%	Percentage polarization	ESMR - Channels T_B^h and T_B^v

where n denotes the n -th observation in the data group, x_i is the i^{th} parameter, x_j is the j^{th} parameter, N is the total number of observations, \bar{x}_i is the mean of the i -th parameter, and \bar{x}_j is the mean of the j -th parameter.

Multiple correlation coefficients were defined as

$$R[x_k(x_j, x_i)] = \left\{ \frac{r(x_k, x_i)^2 + r(x_k, x_j)^2 - 2r(x_k, x_i)r(x_k, x_j)r(x_i, x_j)}{1 - r(x_i, x_j)^2} \right\} \quad (3.2)$$

where x_i , x_j and x_k denote three separate parameters listed in Table 3.1. Linear correlation coefficients for different pairs of parameters, as defined in Eq. 3.1, are denoted by $r(x_i, x_j)$, $r(x_j, x_k)$, $r(x_i, x_k)$ and the i , j , k indexes denote the parameters listed in Table 3.1 that are numbered from 1 to 19. Table 3.1 also identifies the symbols that will be used to identify each parameter in the discussion of results. Also, the notation for linear and multiple correlation coefficients is presented as $r(x_i, x_j)$ and $R[x_k(x_j, x_i)]$, respectively.

Linear and multiple correlation computation results were printed out in a 13 by 13 array for Group 1 data and in a 19 by 19 array for Group 2 data. Figure 3.3 schematically illustrates an array display. Appendix B contains samples of linear and multiple correlation coefficient computation result arrays. It should be noted that arrays of multiple correlation coefficients in Appendix B are values for $R^2[x_k(x_j, x_i)]$.

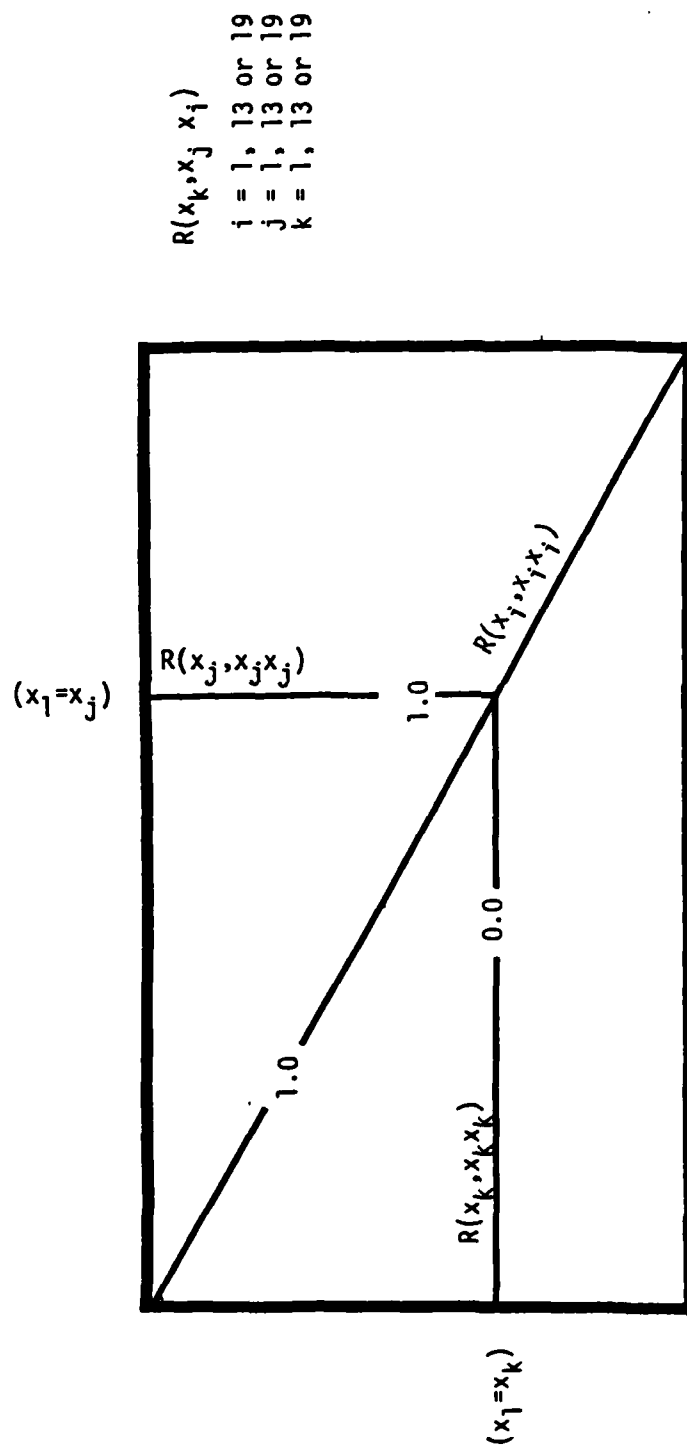


Figure 3.3. Multiple correlation coefficients array.

CHAPTER IV

RESULTS

In order to obtain an overview of the statistical analysis, some general results from the SCAMS data will be presented first. These include comparisons between the five channels of microwave brightness temperatures from the SCAMS experiment as well as comparisons between satellite temperature retrievals and rawinsonde observations for the two data groups. Discussion of these results will be followed by a statistical analysis of the Nimbus VI measurements and conventional meteorological parameters for different cloud and precipitation types that were associated with the mid-latitude cyclone.

Table 4.1 lists the correlation coefficients for the microwave brightness temperatures obtained from channel 1 (T_{B1}) of the SCAMS instrument with brightness temperatures from the other four channels for the two data groups described in Chapter III. The values of the correlation coefficients for these data samples appeared to be very reasonable. As expected, the correlations between the water vapor channel and the atmospheric window channel were very high and amounted to .966 and .965, respectively. Both of these channels detected radiation primarily from the earth's surface because these two channels are dependent on the first term on the right-hand-side of Eq. 2.1. These high correlations suggest there is very little difference in the radiative characteristics of the earth's surface and atmosphere

Table 4.1. Linear correlation coefficients for all cases for SCAMS brightness temperatures for two data groups.

	T_{B1}	T_{B2}	T_{B3}	T_{B4}	T_{B5}	Data Group	No. of Cases
T_{B1}	1.000	.966	.871	.673	-.634	1	273
T_{B1}	1.000	.965	.865	.660	-.727	2	61

between the 1.350 and 0.948 cm wavelength regions.

Correlations of the water vapor channel with the three oxygen channels in Table 4.1 were less because the atmospheric radiation was the primary contributor to the 0.55 cm wavelength region and surface effects were less important. It was interesting to find negative correlation values for $r(T_{B1}, T_{B5})$ in both data groups. These may be attributed to the cold core synoptic systems that were present over the North American Continent at this time when positive temperature anomalies in the lower stratosphere, where channel 5 was most sensitive, were associated with negative temperature anomalies in the lower troposphere where channel 1 was most sensitive.

Since the water vapor and window channels were primarily dependent on the radiative characteristics of the earth's surface, correlation coefficients were computed for surface temperatures (obtained from rawinsonde data) with T_{B1} and T_{B2} . Table 4.2 shows the computational results for the two groups of data. Group 1 data correlations of $r(T_{SFC}, T_{B1})$ were considerably less than Group 2. Although time differences between rawinsonde observations and Nimbus VI passes were

Table 4.2. Linear correlation coefficients between SCAMS brightness temperatures and surface temperatures from rawinsonde observations.

	T_{B1}	T_{B2}	Data Group	No. of Cases
T_{SFC}	.553	.577	1	273
T_{SFC}	.798	.841	2	61

up to 7 hours, it is doubtful this could explain the differences because this problem exists in both data sets. More likely there were different areas sampled in these two groups, with Group 2 more limited and confined to observation times near local noon. Group 1, however, included nighttime observations as well as daytime and effects of diurnal variations will be considered later in this chapter.

A comparison of 500 mb temperatures from rawinsonde was made with brightness temperatures from channels 3 and 4 of SCAMS as well as with 500 mb temperatures derived from the satellite temperature retrievals as shown in Table 4.3. Higher correlations were obtained with T_{B4} for both groups of data. This shows that T_{B3} was more closely weighted to the mid-tropospheric level than was T_{B4} . The very high values for $r(T_{500}, T_{500S})$ of .867 for Group 1 and .904 for Group 2 data corresponded to standard errors of estimates of 3.184 and 3.177°K, respectively, and were considered to be rather large. Different factors contributing to these standard errors could not be entirely due to the differences in observation times but may include the influences of clouds and moisture as well as variations of surface

Table 4.3. Linear correlation coefficients of 500 mb temperatures obtained from rawinsonde observations and SCAMS temperature retrievals.

	T_{500}	T_{500S}	Data Group	No. of Cases
T_{B3}	.801	.832	1	273
T_{B3}	.889	.874	2	61
T_{B4}	.671	.721	1	273
T_{B4}	.752	.746	2	61
T_{500}		.867	1	273
T_{500}		.904	2	61

emissivities. These will be considered in the next section.

Comparisons between the brightness temperatures from the 5 channels of the SCAMS instrument and between SCAMS and conventional observations were reasonable and expected. Variations noted between Group 1 and Group 2 data are mainly due to the differences in the number of cases involved, time frame constraints and changes in the synoptic situation.

Surface, Cloud and Precipitation Effects on SCAMS Measurements

Both Group 1 and Group 2 were divided into subgroups according to different meteorological conditions in order to consider the effects of clouds and moisture on the microwave measurements from SCAMS. The subgroups included cases with clear and overcast

conditions and cases with and without precipitation. Correlation coefficients were computed for each subgroup as well as for all cases together for comparison. The results are shown in Tables 4.4 and 4.5. Values for $r(T_{B1}, T_{SFC})$ and $r(T_{B2}, T_{SFC})$ in Group 1 and 2 data sets showed considerable variation between the highest correlations for cases where precipitation was present and lowest correlations for cases with clear skies. A possible explanation for this was the influence of the microwave radiation from the ground. For the subgroup with precipitation only, the ground was undoubtedly moist for all the cases in the data set, whereas the subgroup with clear skies included moist as well as dry soil cases. Therefore, differences in the T_{B1} temperatures for precipitation cases may be explained primarily by differences in T_{SFC} while variations in T_{B1} for clear cases may be explained by differences in soil emissivities as well as T_{SFC} .

Comparisons of T_{SFC} with T_{B1} and T_{B2} as well as T_{500} with T_{500S} are shown as scattergrams in Figs. 4.1a, 4.1b, and 4.1c for the

Table 4.4. Linear correlation coefficients for Group 1 data set for clear and overcast conditions and cases with and without precipitation.

	$r(T_{B1}, T_{SFC})$	$r(T_{B2}, T_{SFC})$	$r(T_{500}, T_{500S})$	No. of Cases
Clear Sky	.472	.527	.914	91
No Precip.	.515	.532	.891	230
All	.553	.577	.867	273
Overcast	.660	.674	.863	91
Precip.	.739	.805	.836	43

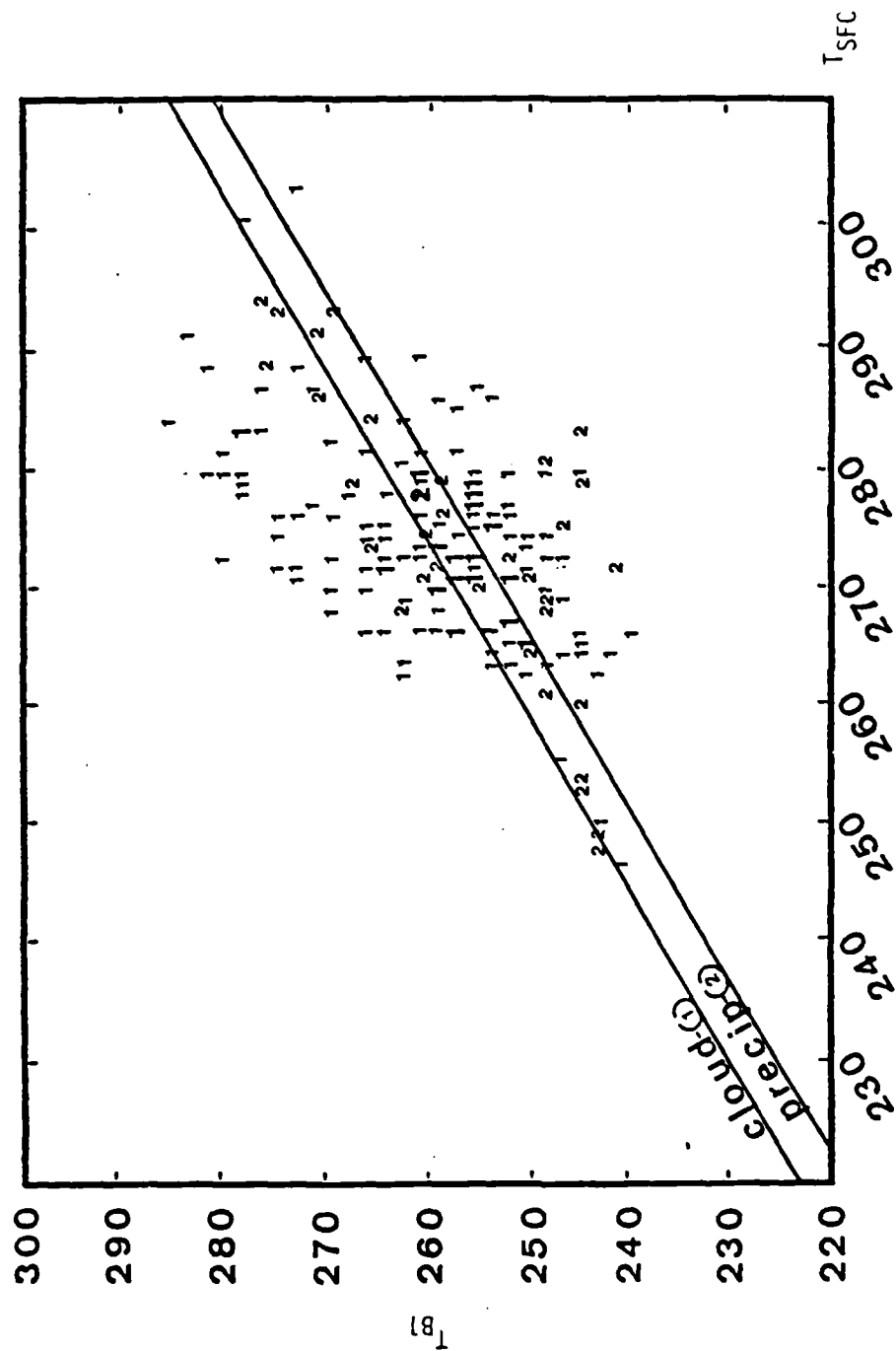


Figure 4.1a. Temperature ($^{\circ}\text{K}$) comparisons of the cloud and precipitation cases for conventional and SCAMS data between T_{SFC} and T_{B1} . Large symbols denote more than one case of data point.

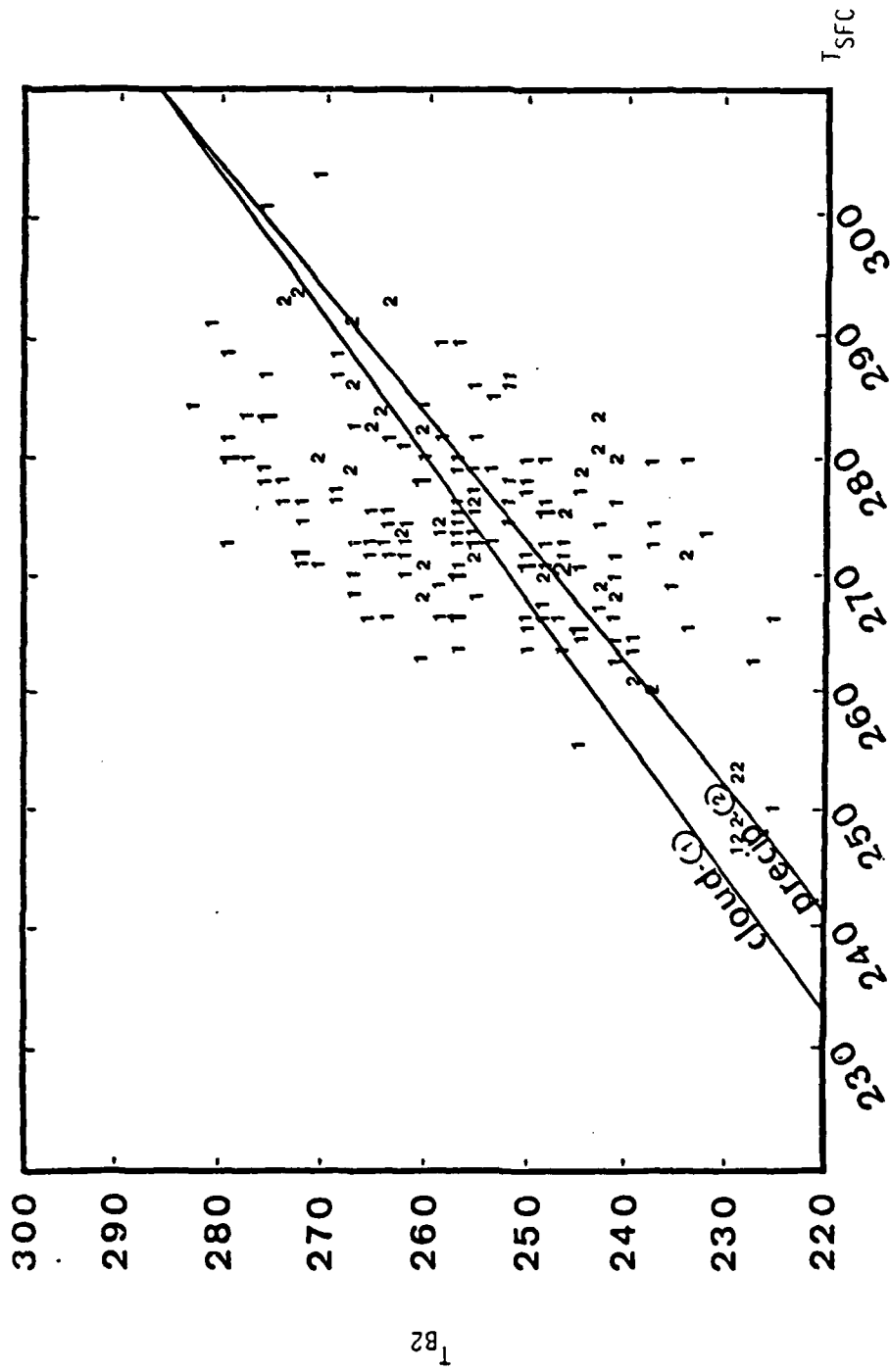


Figure 4.1b. Temperature ($^{\circ}\text{K}$) comparisons of the cloud and precipitation cases for conventional and SCAMS data between T_{SFC} and T_{B2} . Large symbols denote more than one case of data point.

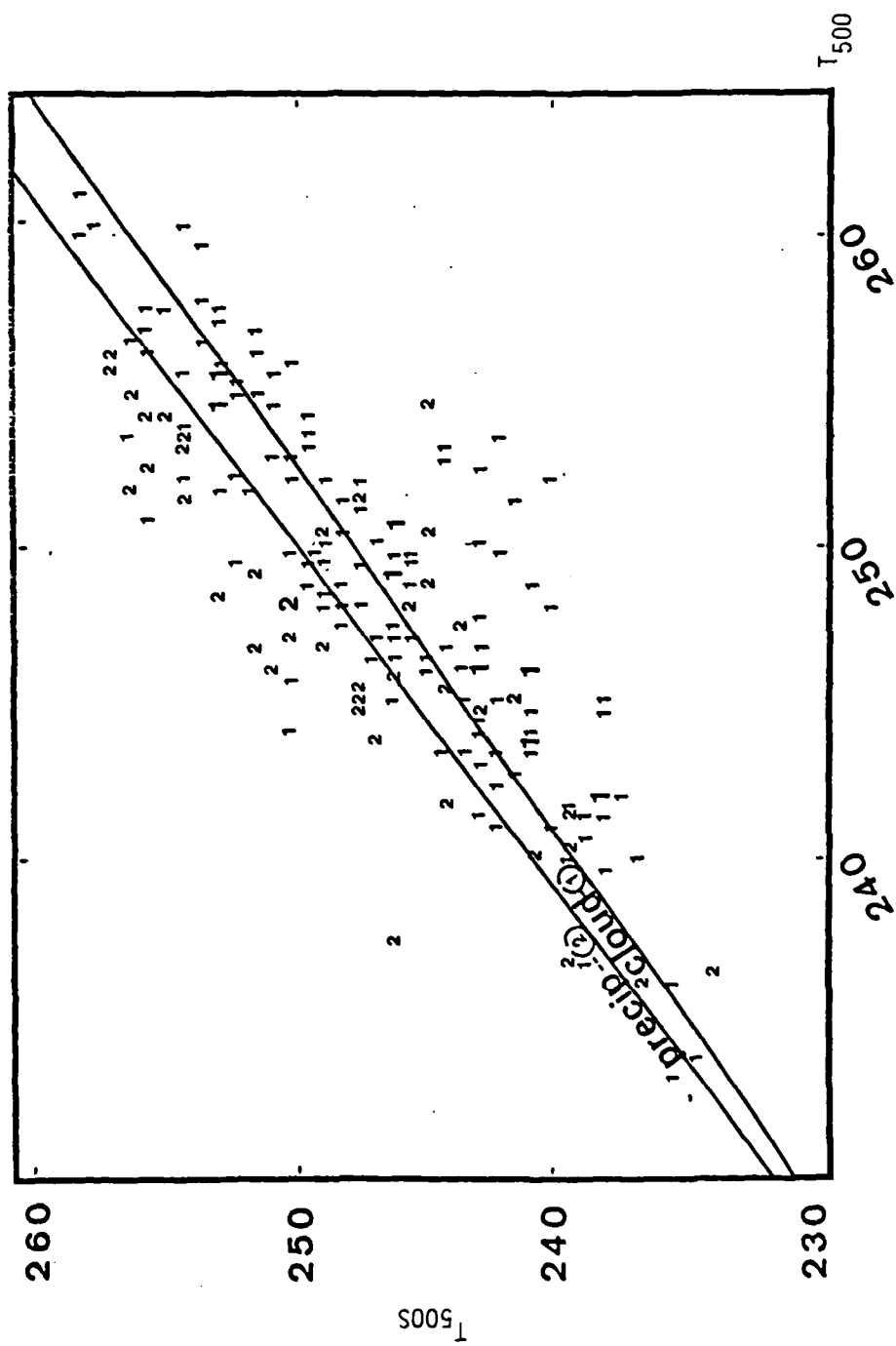


Figure 4.1c. Temperature ($^{\circ}\text{K}$) comparisons of the cloud and precipitation cases for conventional and SCAMS data between T_{500} and T_{500S} . Large symbols denote more than one case at data point.

overcast cloud and precipitation subgroups from the Group 1 data set. The linear regression lines are also included for each subgroup. It was evident from each diagram in Fig. 4.1a and 4.1b, that for a given temperature of T_{SFC} , the channel 1 and 2 brightness temperatures was 3° to 7°K less for precipitation cases than for non-precipitating overcast cloud cases. These temperature differences compared with standard errors of estimate of 9.84°K for the cloud cases and 7.24°K for the precipitation cases. Therefore, it is apparent that it would not be possible to identify a precipitating cloud from a non-precipitating cloud over land with only T_{B1} and T_{B2} remote sensing information.

Correlation values of $r(T_{500}, T_{500S})$ for both Group 1 and Group 2 in Tables 4.4 and 4.5 were rather high and did not show substantial differences between clear skies and precipitation cases. This may be explained by the dependency of T_{500S} on the three oxygen channels which are less sensitive to surface effects than the water vapor and

Table 4.5. Linear correlation coefficients for Group 2 data set for clear and overcast conditions and cases with and without precipitation.

	$r(T_{B1}, T_{SFC})$	$r(T_{B2}, T_{SFC})$	$r(T_{500}, T_{500S})$	No. of Cases
Clear Sky	.561	.621	.900	4
No Precip.	.780	.821	.903	55
All	.798	.841	.904	61
Overcast	.854	.887	.955	23
Precip.	.924	.949	.921	6

window channels on the SCAMS instrument. Correlations of $r(T_{500}, T_{500S})$ for Group 2 range from .900 for clear cases to .955 for overcast cases; however, the data sample was very small with less than 10 cases each for clear sky and precipitation conditions.

The larger data sample for Group 1 for $r(T_{500}, T_{500S})$ in Table 4.4 may be more representative. In this subgroup, the correlation coefficients were highest (.914) for clear cases in a data sample of 91 cases and were lowest (.836) for precipitation with 43 cases. This suggests that 500 mb temperature retrievals for areas with precipitation were less accurate than temperature retrievals from clear sky situations. Effects of the presence of liquid water in the atmosphere in these microwave measurements over land is clearly evident from the data shown in Table 4.4.

The scattergram of T_{500} and T_{500S} in Fig. 4.1c, where precipitation cases and non-precipitating clouds are identified, shows the satellite temperature retrievals for 500 mb were approximately 3°K too low for the overcast cases compared to rawinsonde observations. Standard errors of estimate were 3.417°K for the precipitation cases and 2.979°K for the cloud cases. The T_{500S} values for precipitating cases tended to be too high when 500 mb temperatures exceeded 250°K. These differences may be explained by relatively warm mid-tropospheric air associated with the precipitating clouds compared to colder air associated with the non-precipitating for this mid-latitude cyclone. This problem will be dealt with in more detail later in this section.

Information about effects of snow and rain on the water vapor and window channels of SCAMS were apparent from the scattergrams shown in Figs. 4.2a, b, and c. Plots of T_{SFC} with channels 1 and 2

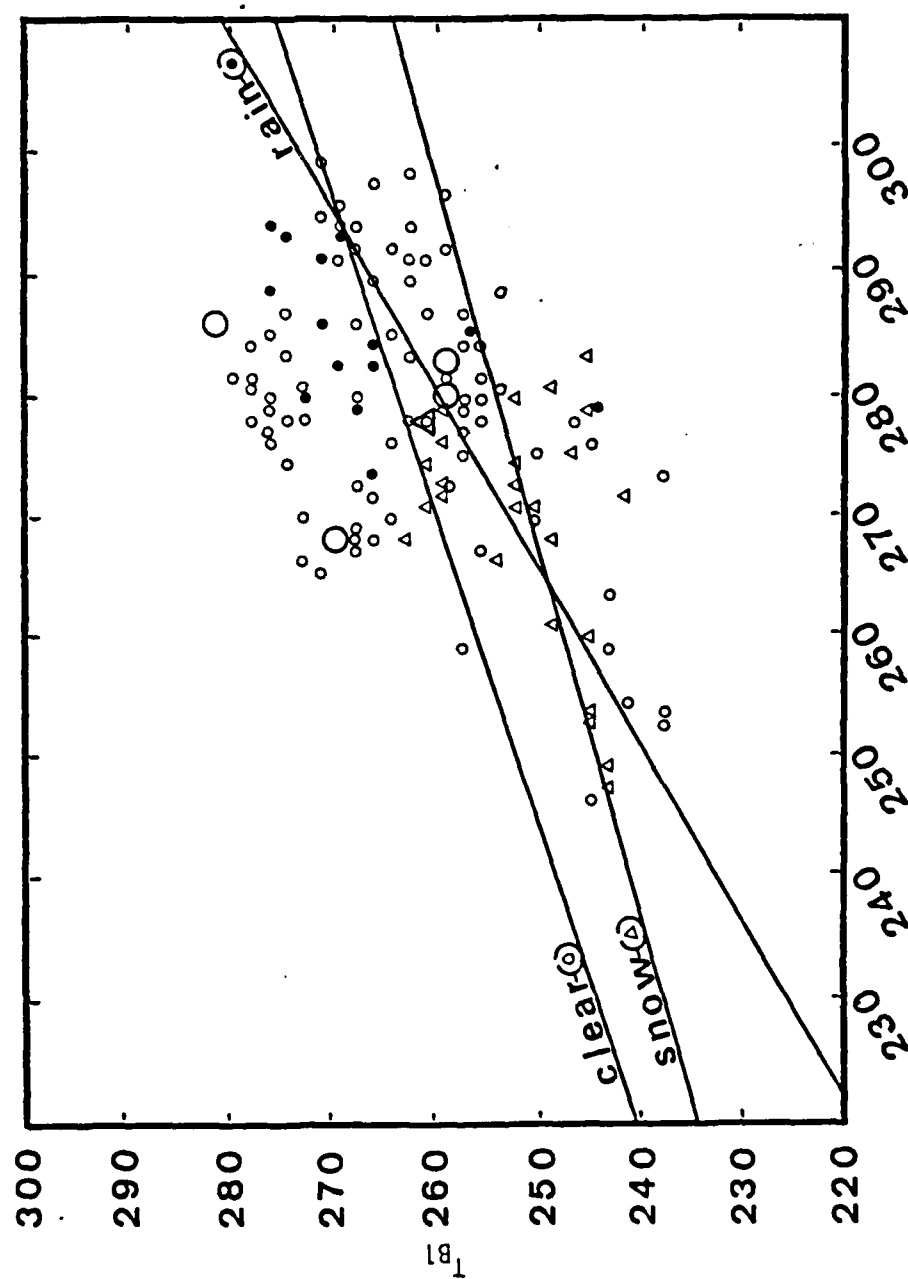


Figure 4.2a. Temperature ($^{\circ}\text{K}$) comparisons of clear, snow and rain cases for conventional and SCAMS data between T_{SFC} and T_{B1} . Large symbols denote more than one case at data point.

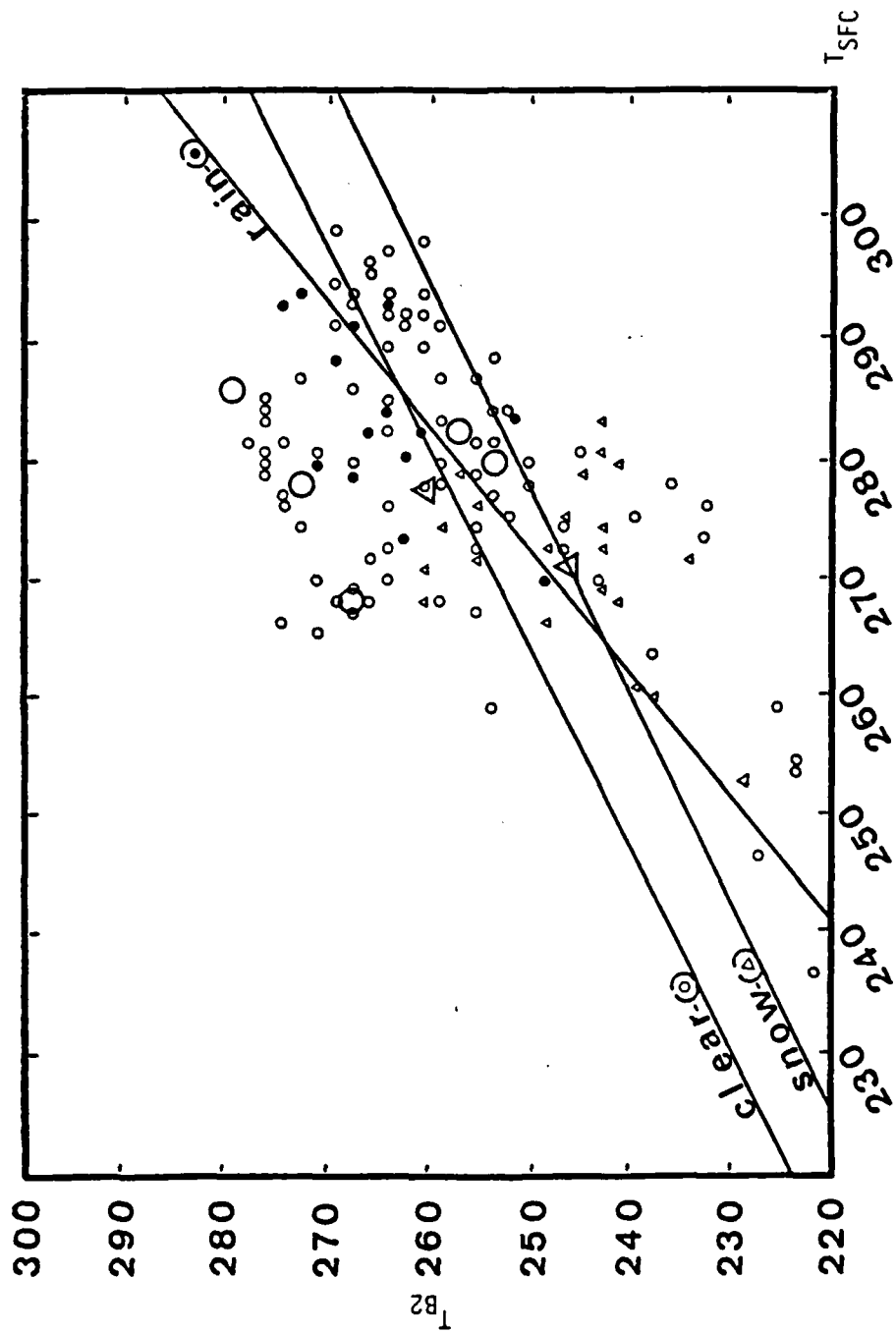


Figure 4.2b. Temperature ($^{\circ}\text{K}$) comparisons of clear, snow and rain cases for conventional and SCAMS data between T_{SFC} and T_{B2} . Large symbols denote more than one case at data point.

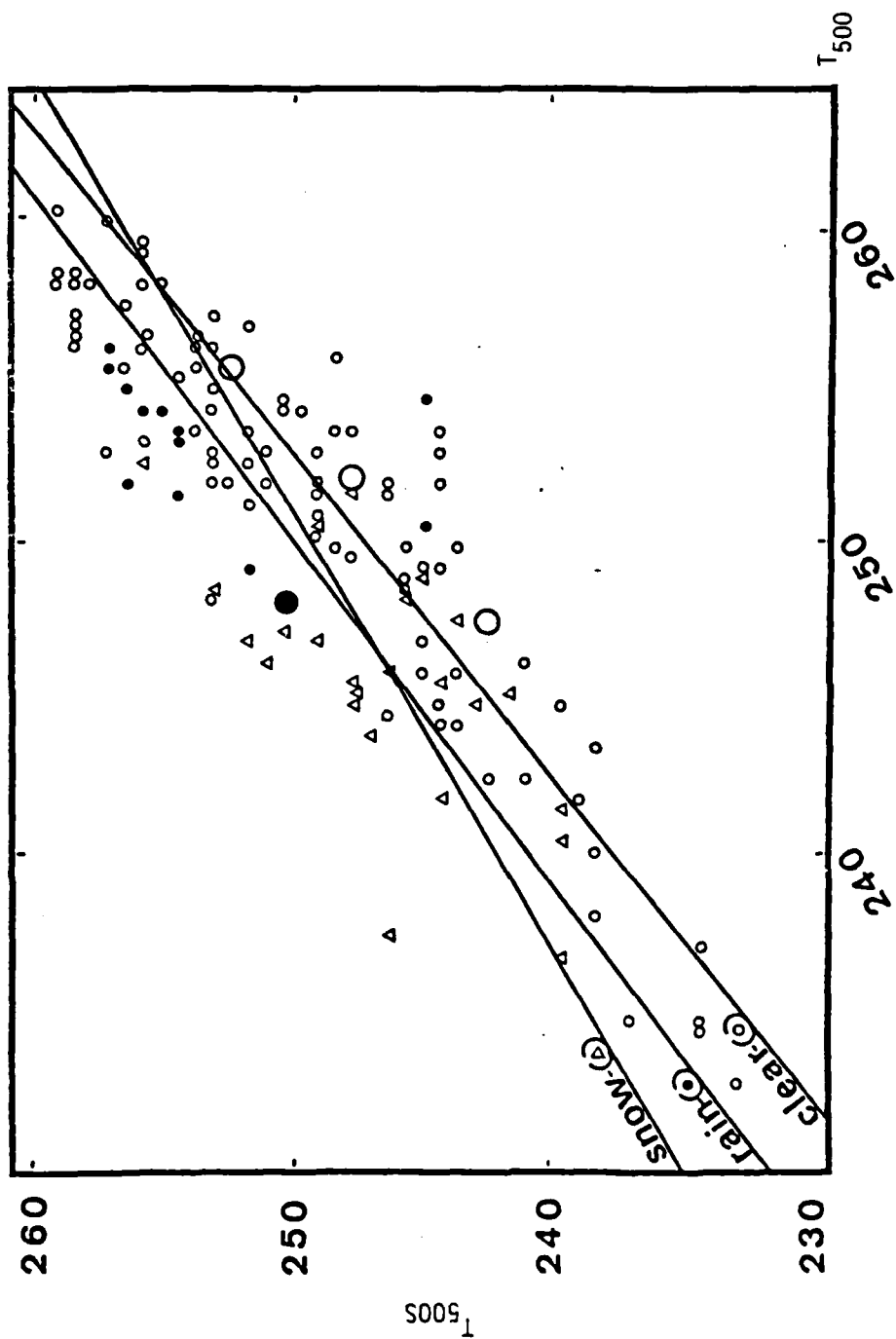


Figure 4.2c. Temperature ($^{\circ}\text{K}$) comparisons of clear, snow and rain cases for conventional and SCAMS data between T_{500} and T_{500S} . Large symbols denote more than one case at data point.

brightness temperatures revealed a well defined clustering of data points with rain for $T_{SFC} > 275^{\circ}\text{K}$ when $T_{B1} > 264^{\circ}\text{K}$ and $T_{B2} > 260^{\circ}\text{K}$ while snow cases were confined to threshold temperatures less than these values. It was also interesting to find some rain cases with values for T_{B1} and T_{B2} almost as high as for clear cases. In addition, comparisons of T_{500S} with T_{500} in Fig. 4.2c show in general that $T_{500S} > T_{500}$ for rain cases while $T_{500S} < T_{500}$ for clear cases; however, the points were widely scattered.

Surface observations and radar summaries were used to distinguish between light and moderate precipitation intensities from the 14 cases shown with rain in Fig. 4.2. Scattergrams similar to Fig. 4.2 were plotted with rain intensity identified for each case (Figs 4.3a, b and c). It was evident that moderate intensity rain was associated with higher microwave brightness temperatures than the light intensity rain. In order to consider possible influences of vertical temperature profiles on these brightness temperatures, the rawinsonde observations were plotted for each case. Nearly all of the cases were located in the area where the strongest rising motions were computed by Hall (1979) over the eastern United States as shown in Fig. 4.4.

Three cases were selected where rising motions were present at mid-tropospheric levels to produce sufficiently thick clouds. These stations included Nashville (72327) and Monett (72349) for 1200 GMT 21 February and are noted in Fig. 4.4. Centerville (72229) was selected for 1200 GMT 22 February and all three rawinsonde observations are shown in Fig. 4.5. In general, all three stations were characterized by low level stability with an inversion and relatively

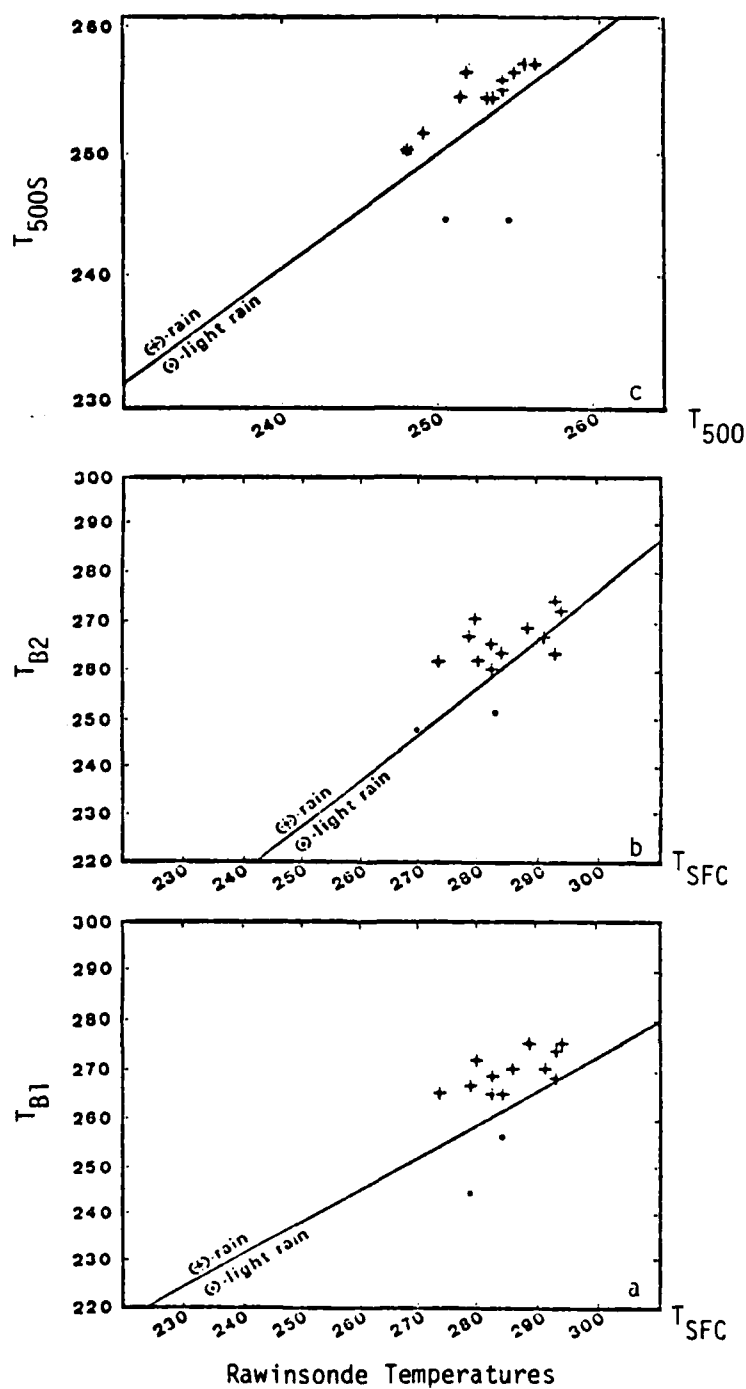


Figure 4.3. Temperature ($^{\circ}\text{K}$) comparisons of the rain cases for conventional and SCAMS data between (a) T_{SFC} , T_{B1} (b) T_{SFC} , T_{B2} and (c) T_{500} , T_{500S} . Line of best fit was for all precipitation (rain and snow) cases to indicate where rain occurred relative to the data set.

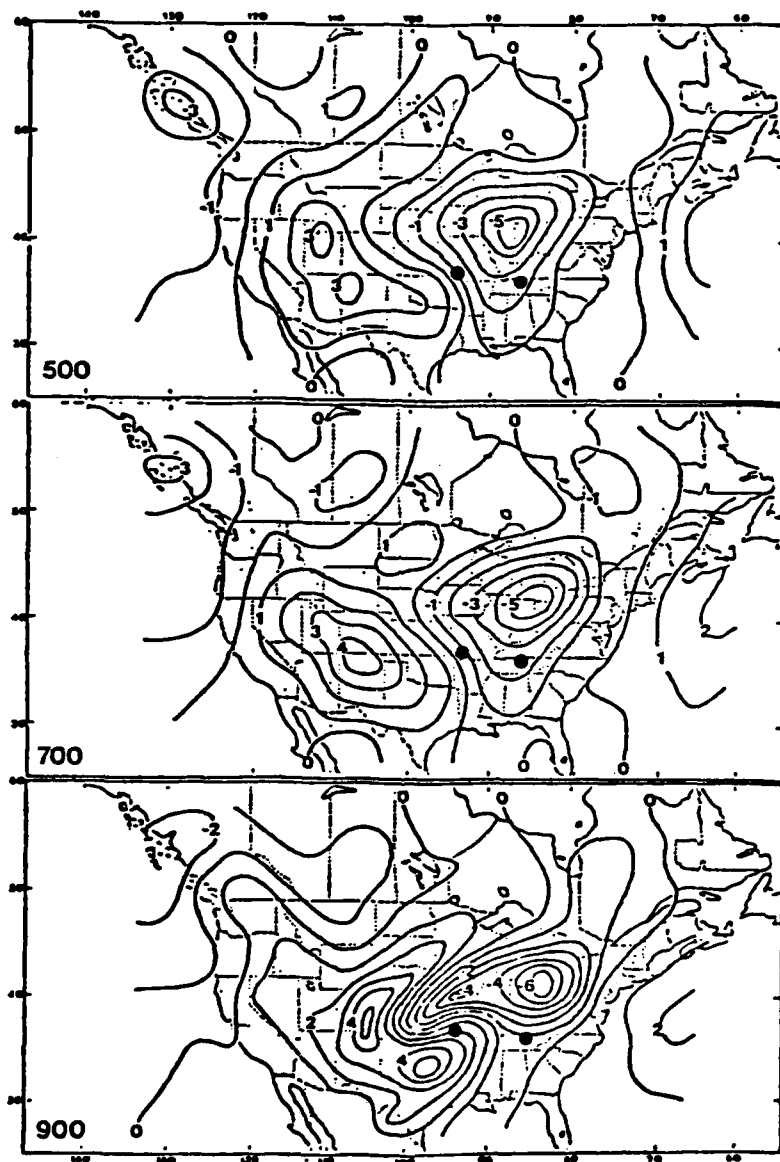


Figure 4.4 Total vertical motions for the 900, 700 and 500 mb levels at 1200 GMT 21 February 1976. Isopleth interval is $1 \mu\text{b s}^{-1}$. Dots show location of rawinsonde stations 72327, BNA-Nashville, Tn. and 72349, UMN-Monett, Mo.

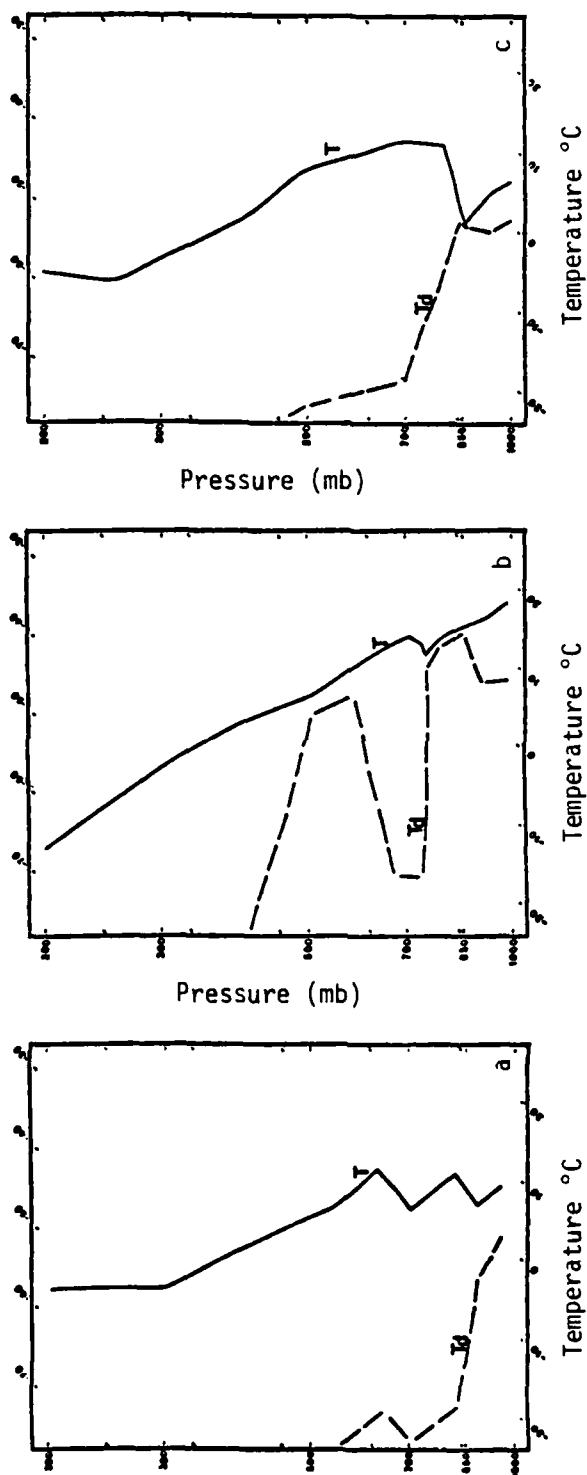


Figure 4.5. Rawinsonde soundings for (a) 72349, UMN-Monett, Mo. (b) 72327, BNA-Nashville, In., at 1200 GMT 21 February 1976 and (c) 72229, CKL-Centerville, Al. at 1200 GMT 22 February 1976.

warm air at mid-tropospheric levels. Since the rawinsonde observations shown in Fig. 4.5 were obtained at 1200 GMT, the data may not exactly coincide with the time of the Nimbus VI orbital pass. This was apparent in the moisture profile for Nashville which was located ahead of a rapidly advancing convective precipitation area at 1200 GMT. However, temperature changes were very small at Nashville as was evident in the 500 mb analysis for this time (Fig. 2.8).

The temperature profiles shown in Fig. 4.5 indicate the warm mid-tropospheric temperatures in the area of ascending motions could contribute to relatively warm brightness temperatures shown in Fig. 4.3. Strong rising motions could support large water droplets which may have a noticeable contribution to the microwave radiation in these spectral regions.

The effects of different cloud types were considered next for non-precipitating overcast conditions. Groups 1 and 2 were divided into three overcast cloud categories which included 1) high clouds only, 2) middle and low clouds, and 3) low clouds only. Also, clear cases with relative humidities less than 25% were considered for the purpose of comparison. Linear correlation coefficients for each of these different non-precipitating cloud categories together with the clear case category were computed and are shown in Tables 4.6 and 4.7. There were more than 60 cases for each category in the Group 1 data set while there were only 17 cases or less for each in Group 2.

It is evident from Tables 4.6 and 4.7 that in general, highest values for $r(T_{B1}, T_{SFC})$ and $r(T_{B2}, T_{SFC})$ were found for low cloud categories and amounted to approximately .70 for the Group 1 data set where there was a substantial number of cases. There was progressively

Table 4.6. Linear correlation coefficients for Group 1 data set for clear cases with relative humidities less than 25% and non-precipitating overcast conditions for low, middle, and high clouds.

	$r(T_{B1}, T_{SFC})$	$r(T_{B2}, T_{SFC})$	$r(T_{500}, T_{500S})$	No. of Cases
Clear RH-25%	.510	.554	.913	69
Overcast High Cloud	.657	.636	.852	61
Overcast Low & Mid Cloud	.694	.702	.841	80
Overcast Low Cloud	.708	.711	.841	66

Table 4.7. Linear correlation coefficients for Group 2 data set for clear cases with relative humidities less than 25% and non-precipitating overcast conditions for low, middle, and high clouds.

	$r(T_{B1}, T_{SFC})$	$r(T_{B2}, T_{SFC})$	$r(T_{500}, T_{500S})$	No. of Cases
Clear RH \leq 25%	.491	.556	.913	3
Overcast High Cloud	.839	.875	.947	17
Overcast Low & Mid Cloud	.862	.849	.930	17
Overcast Low Cloud	.871	.860	.936	15

smaller correlation values for middle and high cloud categories where correlation values were approximately .65 for high overcast conditions. In comparison, the correlations for clear cases were less than .56. These results suggest that cloudiness does have an effect on microwave brightness temperatures even in the absence of precipitation, especially for low level clouds where the liquid water content would be greater compared to high level clouds. It was interesting to note that correlation coefficient values for low overcast conditions were similar to the one for precipitation cases shown in Table 4.4. Perhaps moist soil conditions may be associated with the low overcast cases in Table 4.6.

Comparisons of 500 mb temperature retrievals with rawinsonde observations were also made for the different cloud categories and correlation coefficients of $r(T_{500}, T_{500S})$ were computed from Groups 1 and 2 data sets given in Tables 4.6 and 4.7. In the Group 1 data set,

overcast cases produced lower values for $r(T_{500}, T_{500S})$ than clear cases and amounted to .913 compared to .841 for low and middle overcast skies. From these results, it is apparent that the liquid water content of the non-precipitating clouds for this wintertime synoptic situation was high enough to somewhat degrade the satellite temperature retrievals at mid-tropospheric levels. It was not possible to draw any conclusions from the values of $r(T_{500}, T_{500S})$ in the Group 2 data set because of the limited number of data in each cloud category.

Because there was a reasonable number of cases in the Group 1 data set shown in Table 4.6 for the different cloud categories, multiple correlation coefficients were computed from Eq. 3.2. Values of $R[T_{B1}, (T_{SFC}, T_{B2})]$ determined the proportion of channel 1 brightness temperatures (T_{B1}) variations accounted for by the linear influence of surface temperature observations (T_{SFC}) and channel 2 brightness temperature (T_{B2}). The results of the computations of multiple correlation coefficients are listed in Table 4.8.

It can be seen when values of $R[T_{B1}, (T_{SFC}, T_{B2})]$ in Table 4.8 are compared with values of $r(T_{SFC}, T_{B2})$ in Tables 4.4 and 4.6 for Group 1 data, there is a somewhat larger value for the multiple correlation coefficients. For example, with precipitation cases $r(T_{B1}, T_{SFC}) = .739$ and $R[T_{B1}, (T_{SFC}, T_{B2})] = .811$ while for clear sky cases $r(T_{B1}, T_{SFC}) = .472$ and $R[T_{B1}, (T_{SFC}, T_{B2})] = .532$. This result was expected, however, because of high correlation between T_{B1} and T_{B2} as previously noted. These results indicate the need for more accurate surface temperature measurements that were not possible in precipitating clouds over land areas at the 1.350 and 0.948 cm microwave regions from the SCAMS measurements.

Table 4.8. Multiple correlation coefficients for Group 1 between SCAMS brightness temperatures from channel 1 with surface temperature measurements from rawinsonde measurements and channel 2 data.

	$R[T_{B1}(T_{SFC}, T_{B2})]$	No. of Cases
No Precip.	.532	230
Clear Skies	.558	92
All Cases	.577	273
Overcast/High Cloud	.657	61
All Overcast Cases	.675	91
Overcast/Low & Mid	.706	80
Overcast/Low	.716	66
Precip.	.811	43

Terrain Effects on Data from SCAMS

Previous studies have shown that terrain height was a factor that also contributed to variations in microwave brightness temperatures in SCAMS measurements (Staelin, et al., 1975). Since terrain elevation was included with each SCAMS data point location on the Nimbus VI data tapes, it was possible to consider this factor in the statistical analyses. Only Group 1 data set was used because of the sample size. Four subgroups were chosen to represent different ranges of elevations and these are identified in Table 4.9. One subgroup included only data with terrain heights less than 500 meters, the second subgroup contained data for terrain heights between 500 and 1000 meters, the third subgroup consisted of data between 1000 and 2000 meters, and the fourth subgroup included all data above 2000 meters. Each subgroup

contained more than 30 data points to provide an adequate sample for statistical analyses.

Correlation coefficients between brightness temperatures obtained from channels 1 and 2 of SCAMS and conventional temperature observations are shown in Table 4.9. Highest correlations for $r(T_{B1}, T_{SFC})$ and $r(T_{B2}, T_{SFC})$ were obtained for the subgroup with terrain heights less than 500 meters and amounted to approximately .700. At higher elevations, above 1000 meters, the correlations were very small (less than .100) and may be attributed to snow cover over the mountainous regions during February, 1976. Previous studies have noted low emissivities for snow in the microwave spectral (Wilheit, *et al.*, 1976). Degradation of 500 mb temperature retrievals at higher elevations in the SCAMS data are clearly evident from values of $r(T_{500}, T_{500S})$ that are shown in Table 4.9.

Because of the importance of terrain elevations shown in Table 4.9, multiple correlations were computed for selected parameters

Table 4.9. Linear correlation coefficients between channel 1 brightness temperatures and rawinsonde surface temperatures for different terrain heights from Group 1 data.

Terrain Heights (m)	$r(T_{B1}, T_{SFC})$	$r(T_{B2}, T_{SFC})$	$r(T_{500}, T_{500S})$	No. of Cases
TER < 500	.683	.711	.909	116
500 ≤ TER < 1000	.623	.713	.918	52
1000 ≤ TER < 2000	.092	.061	.900	73
TER > 2000	.001	.033	.776	32

where terrain effects were included. Values for $R[T_{B1}, (T_{SFC}, TER)]$ and $R[T_{500}, (T_{500S}, TER)]$ were obtained for precipitation cases and different cloud categories to find if there were any substantial increases in the correlations. The results are listed in Table 4.10.

It is evident that the correlations were higher for the T_{500} and T_{500S} comparisons for precipitating and non-precipitating cases as well as for all of the cases in Group 1. For example, $r(T_{500}, T_{500S})$ was .867 and compared to a value of .915 for $R[T_{500}, (T_{500S}, TER)]$. However, only a small increase was found when T_{B1} was compared with T_{SFC} after terrain was included in the multiple correlation. Possibly the weighting functions used to obtain T_{500S} in the Nimbus VI retrieval scheme for the oxygen bands, as shown in Fig. 2.1, were not representative of high mountainous areas.

Diurnal Temperature Variations in SCAMS Measurements

Since SCAMS measurements were available twice a day with observation times near local noon and local midnight throughout the period of study, it was possible to consider the diurnal fluctuations of brightness temperatures in the fine microwave channels of the SCAMS experiment. It is well known that diurnal temperature variations are relatively large for clear weather and small for cloudy weather or whenever precipitation occurs (Trewartha, 1954). For this reason, average brightness temperatures for the two subgroups of clear and precipitation cases within Group 1 data set were obtained for all of the northbound (local noon) passes and for all of the southbound (local midnight) passes. Table 4.11 list these average temperatures for all five of the SCAMS channels. The corresponding rawinsonde temperatures

Table 4.10. Linear and multiple correlation coefficients of SCAMS measurements and conventional observations to show terrain effects for Group 1 data set.

	$r(T_{B1}, T_{SFC})$	$R[T_{B1}, (T_{SFC}, TER)]$	$r(T_{500}, T_{500S})$	$R[T_{500}, (T_{500S}, TER)]$	No. of Cases
Clear Skies	.472	.473	.914	.940	92
All Cases	.553	.555	.867	.915	273
Non-precip Overcast	.660	.683	.863	.903	230
Precip.	.739	.750	.836	.921	43

for 0000 and 1200 GMT are given for these cases for a comparison with conventional observations.

Tables 4.11a and b show that conventional surface temperatures were, as expected, warmer for the local late afternoon hours (0000 GMT) than during the local early morning hours (1200 GMT) for both the clear and precipitation cases and amounted to 7.8°K for clear cases and 3.1°K for precipitation cases. In comparison, SCAMS brightness temperatures near local midnight were cooler than the temperatures obtained near local noon. The temperature differences for clear cases were 11.6°K for T_{B1} and 14.6°K for T_{B2} . Diurnal temperature variations were also quite evident for T_{B3} in Table 4.11a but were practically negligible for the other two oxygen channels where T_{B4} and T_{B5} differences were less than the instrument noise level. Contributions to brightness temperature of the channel 3 oxygen band due to surface effects is clearly evident from the T_{B3} temperature difference for clear cases.

These results show the SCAMS instrument sensitivity to surface soil temperatures. According to Geiger (1965) the maximum surface soil temperatures occur approximately 1 1/2 hours after the insolation maximum while minimum soil temperatures occur near sunrise for an average wintertime day. Diurnal fluctuations of air temperatures from conventional meteorological observations at approximately 5 feet above the surface, lag the ground temperatures by 1/2 to 1 1/2 hours and explain why the air for clear cases was warmer at 0000 GMT than 1200 GMT from rawinsonde observations over the U.S. but colder near local midnight (Nimbus VI southbound pass) than around local noon

Table 4.11. Average brightness temperatures ($^{\circ}\text{K}$) from SCAMS data for observation times near local midnight (05 to 08 GMT) and local noon (15 to 19 GMT) over the North American Continent for a) clear cases only and b) precipitation cases. Average surface temperatures from collocated rawinsonde stations are included to provide information about diurnal variations from conventional data.

Observation Time (Nimbus VI)	No. of Cases	T_{B1}	T_{B2}	T_{B3}	T_{B4}	T_{B5}	T_{SFC} (Rawinsonde)
Near local midnight (05 to 08 GMT)	54	256.2	252.2	247.9	241.3	219.3	281.6 (00 GMT)
Near local noon (15 to 19 GMT)	39	267.8	266.8	257.0	242.5	218.4	273.8 (12 GMT)
Temperature Difference ΔT		-11.6	-14.6	- 9.1	- 1.2	+ 0.9	+ 7.8

a) Clear cases

b) Precipitation cases

Observation Time (Nimbus VI)	No. of Cases	T_{B1}	T_{B2}	T_{B3}	T_{B4}	T_{B5}	T_{SFC} (Rawinsonde)
Near local midnight (05 to 08 GMT)	18	254.4	249.9	251.7	241.4	221.4	276.0 (00 GMT)
Near local noon (15 to 19 GMT)	25	257.2	252.1	250.9	233.4	220.9	272.9 (12 GMT)
Temperature Difference ΔT		- 2.8	- 2.2	+ 0.8	+ 8.0	+ 0.5	+ 3.1

(Nimbus VI northbound pass) from satellite remote sensing. Moreover, soil temperatures may be more than 15°C warmer than air (Shelter) temperatures for desert areas in the southwestern United States (Kern, 1963).

Average temperatures for precipitation cases in Table 4.11b show much smaller differences between the two observation times when surface temperature variations would be expected to be small. It was surprising to find an 8°K temperature difference for the T_{B4} averages. One possible explanation could be related to the synoptic weather system itself rather than some unknown solar contamination for Nimbus VI measurements near local noon. This problem will need to be investigated in subsequent studies of other synoptic cases.

Comparisons of SCAMS, ESMR, and HIRS Measurements

Statistical analyses were also carried out between conventional meteorological observations and the ESMR and HIRS measurements. In addition, comparisons of these satellite measurements were made with SCAMS data in order to study the effect of precipitation and cloud types in these multispectral wavelength regions. Both ESMR and HIRS measurements of the mid-latitude cyclone were limited to daytime (northbound) orbital passes and, therefore, sample size for these data in Group 2 was more limited than in the one previously discussed.

General results of the linear correlation computations for ESMR compared with SCAMS and conventional meteorological surface temperatures are presented in Table 4.12. Comparisons with T_{SFC} were carried out first because the ESMR instrument primarily sensed the earth's surface and was nearly transparent to the atmosphere. Table 4.12

shows values for $r(T_{AVG}, T_{SFC})$ amounted to .685 for ESMR compared to higher correlations for channels 1 and 2 of SCAMS for 60 cases in the Group 2 data set. Lower correlation values for ESMR may be explained by its greater sensitivity to such factors as soil moisture, snow, and precipitation compared to the SCAMS instrument. It was apparent that the values for $r(T_{B1}, T_{SFC})$ and $r(T_{B2}, T_{SFC})$ in Table 4.12 were too low in this data sample to make it possible to obtain reliable remote sensing measurements of surface temperatures over land for SCAMS for use with ESMR T_{AVG} measurements.

In order to consider the possible effects of cloudiness on the ESMR brightness temperatures, Group 2 data set was divided into six subgroups according to clear and overcast conditions with low, middle, and high cloudiness. Correlation coefficients were computed for each subgroup to find relationships in ESMR brightness temperatures with conventional surface temperatures and brightness temperatures from the

Table 4.12. Linear correlation coefficients between ESMR vertically and horizontally polarized brightness temperature and SCAMS brightness temperature from channel 1 and 2 from Group 2 data.

	T_{B1}	T_{B2}	T_{SFC}	No. of Cases
T_{AVG}	.775	.794	.685	60
T_B^v	.824	.834	.752	
T_B^h	.698	.723	.598	
T_{SFC}	.789	.825		

the window channel (T_{B2}) of SCAMS. The results are given in Table 4.13.

In general, the highest correlations for $r(T_{SFC}, T_{AVG})$ were found for clear sky conditions and amounted to .935 for a data sample with only 9 clear cases in Group 2. Nearly all of these were located within the area from Arizona to Texas where no precipitation had occurred as previously indicated in Figs. 2.9 and 2.10. The soil conditions at these locations were very dry and free of snow. Therefore surface emissivities in the microwave region were very high and were comparable to emissivities at infrared wavelengths. Similar reasons may explain the high correlation value of .968 for $r(T_{B2}, T_{SFC})$.

Correlation values of $r(T_{SFC}, T_{AVG})$ for the three overcast conditions were substantially lower compared to the clear cases. There was very little difference in the correlations for low, middle, and high overcast conditions which suggest that cloud types were not detectable at the ESMR wavelengths. The lower correlation values for overcast cases may possibly be explained by moist soil conditions that were the result of precipitation associated with overcast skies.

It was also interesting to find in Table 4.13 that there were significant differences in $r(T_{SFC}, T_B^V)$ and $r(T_{SFC}, T_B^h)$. Correlations for vertical polarizations were always higher than for horizontal polarizations. Most noteworthy however, was the large difference between T_B^V and T_B^h for the low overcast skies and the low and middle cloud conditions where correlation values for $r(T_{SFC}, T_B^V)$ was .741 while $r(T_{SFC}, T_B^h)$ amounted to .404. It is obvious from Eq. 2.3 that weak but significant polarization was present in the ESMR brightness temperatures and $T_B^V > T_B^h$. As noted by Rogers *et al*, (1974) such conditions as wet soil or snow cover produce a highly polarized

Table 4.13. Linear correlation coefficients for Group 2 for ESMR, SCAMS, and conventional data under different cloud conditions.

	$r(T_{SFC}, T_{AVG})$	$r(T_{SFC}, T_B^V)$	$r(T_{SFC}, T_B^H)$	$r(T_{B2}, T_{AVG})$	$r(T_{B2}, T_{SFC})$	No. of Cases
Clear	.935	.965	.872	.968	.939	9
Broken/overcast	.675	.775	.564	.717	.834	32
Overcast	.681	.798	.572	.723	.868	22
Overcast/low cloud	.532	.740	.411	.609	.860	15
Overcast/low & mid cloud	.553	.741	.404	.619	.849	17
Overcast/high cloud	.539	.704	.412	.598	.871	16

surface when viewed obliquely and may explain these differences found here. It should be noted that for precipitating clouds, microwave radiation in the .81 cm wavelength region of ESMR is unpolarized according to theoretical studies by Weinman and Guetter (1977) and therefore could not explain the difference in values between $r(T_{SFC}, T_B^v)$ and $r(T_{SFC}, T_B^h)$.

Comparisons were made between T_{B2} from SCAMS with the average brightness temperatures from ESMR. The SCAMS channel 2 brightness temperatures were chosen instead of those from channel 1 because the window channel provided more accurate surface temperature measurements than the water vapor channel as shown in correlations of T_{B1} and T_{B2} with T_{SFC} in Table 4.2. The results for $r(T_{B2}, T_{AVG})$ in Table 4.13 are somewhat similar to $r(T_{SFC}, T_{AVG})$ for the different cloud conditions and indicated that T_{B2} was not sensitive to the same surface characteristics as T_{AVG} .

Additional moisture distinctions were considered for the ESMR data by dividing the Group 2 data into precipitating and non-precipitating categories. Out of the 60 cases, only five were associated with precipitation and may not be a large enough sample to give meaningful results.

Table 4.14 gives the correlation coefficients that were computed for the two categories from the Group 2 data set. The percentage of polarization from ESMR measurements was also included as one of the parameters in the computations for the purpose of showing the significant effect surface moisture has in this spectral region. For the precipitation category, distinct differences existed in the

Table 4.14. Linear correlation coefficients for ESMR brightness temperatures and percentage polarization with conventional meteorological data and SCAMS measurements for precipitating and non-precipitating cases.

	$r(T_{SFC}, T_{AVG})$	$r(T_{SFC}, T_B^V)$	$r(T_{SFC}, T_B^h)$	$r(T_{B2}, T_{AVG})$	$r(T_{B2}, T_{SFC})$	$r(T_{SFC}, P\%)$	No. of Cases
Precipitating	-.042	.368	-.178	-.080	.943	.410	5
Non-precipitating	.756	.704	.781	.866	.821	-.080	55

correlation coefficient values between all of the parameters from the three instruments. Even though there were only five precipitation cases, the correlation values appear to be consistent and indicate the sensitivity of ESMR to surface moisture. This displays a potential application of satellite microwave instrumentation to obtain global moisture analyses over land masses.

The correlation coefficient values for the precipitation cases in Table 4.14 for $r(T_{SFC}, T_{AVG})$ amounted to $-.042$ and suggest no correlation. Even with the limited data sample, there appeared to be some difference between the T_B^V and T_B^h correlations with T_{SFC} which indicates these five cases were polarized. Also, $r(T_{SFC}, P\%)$ was $.410$ and was in contrast to the non-precipitating category where $r(T_{SFC}, P\%)$ was only $-.080$. This low negative value was attributed to the presence of a variety of surface and soil properties including snow cover, as well as to the very low percent polarizations (less than 1%) for dry soil conditions. Also, as will be discussed later, the negative value for $r(T_{SFC}, P\%)$ may be due to the small percent polarizations related to warm, dry soil temperatures with high emissivities and large percent polarizations related to relatively cold, moist soil temperatures with low emissivities.

The potential effects of terrain height variations in the ESMR brightness temperature measurements were also investigated. The 60 cases in Group 2 were divided into three subgroups with cases below 500 meter elevations, 2) between 500 and 1000 meters, and 3) above 1000 meters. Correlation coefficients were computed in each of these subgroups for T_{SFC} with T_B^V , T_B^h , T_{AVG} , and $P\%$ and the results are

depicted in Table 4.15.

The dependence of ESMR brightness temperatures on terrain heights was not as evident as was found from SCAMS measurements. Table 4.15 shows $r(T_{SFC}, T_{AVG})$ was .749 for cases below 500 m elevations and was some what smaller for the other two subgroups. The most interesting result was evident in the values for $r(T_{SFC}, P\%)$ which varied from -.232 for terrain heights less than 500 meters to .487 for cases above 1000 meters. The reason for the negative correlation was similar to the one used to explain the negative value for $r(T_{SFC}, P\%)$ in Table 4.14; however, the positive value for high elevations is more difficult to explain. During the wintertime, snow cover is very extensive above 1000 meter elevations and it was possible that dry and "wet" snow surfaces were sensed by the ESMR instrument. At relatively warm temperatures ($\sim 0^\circ\text{C}$), the snow was melting and therefore had "wet soil" like radiative characteristics with low emissivities. At extremely low temperatures at high elevations however, snow-covered terrain was characterized by the absence of liquid water and emissivities were not likely to be as low. Since

Table 4.15. Linear correlation coefficients for Group 2 ESMR and conventional meteorological data for different terrain heights.

Terrain Height	$r(T_{SFC}, T_{AVG})$	$r(T_{SFC}, T_B^V)$	$r(T_{SFC}, T_B^H)$	$r(T_{SFC}, P\%)$	No. of Cases
$TER \leq 500$ m	.749	.821	.676	-.232	26
$500 < TER \leq 1000$ m	.684	.714	.641	-.190	13
$TER > 1000$ m	.631	.668	.542	.487	21

emissivity values are inversely proportional to percent of polarization for wet land, warm surfaces are associated with high polarizations while cold surfaces are associated with low polarizations to result in a positive value for $r(T_{SFC}, P\%)$ for mountainous regions.

Up to this point, conventional meteorological observations have been used to define various cloud and precipitation categories for studying the SCAMS and ESMR data. This statistical method of analysis was extended to include HIRS data which provided digital information primarily about 1) cloud detection from reflected solar radiation (REFL) and 2) cloud top temperatures from equivalent blackbody infrared temperatures (T_{IR}) in the $11\ \mu m$ window region. As explained in detail in Chapter II, the HIRS data were available for the same orbital passes on Nimbus VI as SCAMS and ESMR and therefore were very useful.

Correlation coefficients were computed for REFL and T_{IR} from HIRS with some of the conventional, SCAMS, and ESMR data for Group 2 and are given in Table 4.16. Relatively low positive correlations were found for $r(T_{SFC}, T_{IR})$ and the other parameters correlated with T_{IR} . This may be explained by the sensitivity of T_{IR} to clouds, particularly high level cirrus, and the relative insensitivity of T_{B1} and T_{B2} to clouds. Highest values for T_{IR} occurred when skies were clear and T_{B1} and T_{B2} were also relatively high. Therefore the correlation coefficients were positive.

Correlations of these parameters with HIRS solar reflectance showed small negative correlations. For example $r(T_{B1}, REFL)$ and $r(T_{B2}, REFL)$ amounted to $-.260$ and $-.262$, respectively. This indicates

AD-A092 217

AIR FORCE INST OF TECH WRIGHT-PATTERSON AFB OH
THE INFLUENCE OF CLOUD AND ATMOSPHERIC MOISTURE ON THE STATISTI-EYC(U)
AUG 80 P W SPECK

F/S 4/5

UNCLASSIFIED

AFIT-CI-80-43T

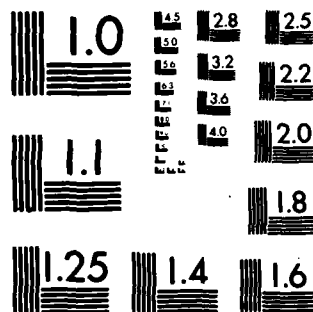
NL

2 of 2

AUG 80



END
DATE
FILMED
1-8
DTIC



MICROCOPY RESOLUTION TEST CHART
NATIONAL BUREAU OF STANDARDS-1963-A

Table 4.16. Linear correlation coefficients of rawinsonde surface and 500 mb temperatures, compared to HIRS equivalent blackbody temperature and reflected solar radiation channel data.

	ESMR				HIRS	
	T_B^v	T_B^h	T_{AVG}	P%	T_{IR}	REFL
T_{SFC}	.752	.598	.685	-.017	.354	-.050
T_{B1}	.824	.698	.775	-.098	.584	-.260
T_{B2}	.834	.723	.794	-.138	.592	-.262
T_{500}	.684	.514	.606	.062	.290	.080
T_{500S}	.746	.597	.682	-.023	.484	-.099
No. of Cases	60				47	

from these data that for cases with low albedoes, such as cloud-free land areas, the microwave brightness temperatures tend to be high if there was dry soil. The correlations were low because some cloud-free areas had wet soil (low emissivities in microwave region) with low T_{B1} and T_{B2} values.

Additional correlations were made with T_{B1} and T_{B2} from SCAMS and REFL from HIRS data for various cloud and precipitation categories as previously discussed. These are identified in Table 4.17 where correlation coefficients are given for $r(T_{B1}, REFL)$ and $r(T_{B2}, REFL)$. It is evident from these results that T_{B1} and T_{B2} with REFL contain correlative information about cloud and precipitation areas. Large negative correlations of $-.592$ and $-.649$ were found for clear

Table 4.17. Linear correlation coefficients of SCAMS surface temperatures and HIRS reflectance measurements clear and overcast conditions and cases with and without precipitation.

	$r(T_{B1}, REFL)$	$r(T_{B2}, REFL)$	No. of Cases
Clear	-.592	-.649	4
Overcast	-.294	-.334	21
No precip.	-.187	-.189	40
All cases	.584	.592	47
Precip.	.658	.637	7

cases compared to -.294 and -.334 for non-precipitating overcast cases. These were in contrast to large positive correlation of .658 and .637 obtained from precipitation cases; however, the data sample was very small and may not necessarily be representative.

The results in Table 4.17 may be interpreted to indicate that, for precipitating clouds with high reflectivities, the apparent microwave brightness temperatures tended to be warmer with thick, highly reflective clouds and colder with lower reflective clouds. Possibly, the precipitating clouds in this wintertime synoptic system could have been warmer than the underlying surface which may also have been moist to reduce the surface microwave emissions.

Analyses of the average microwave brightness temperatures from ESMR helped explain some of the correlative information given in Tables 4.16 and 4.17. Figure 4.6 shows the ESMR brightness temperature for 20 February 1976 and corresponds with GOES visual and infrared satellite images in Figs. 2.11 and 2.12. It is evident that

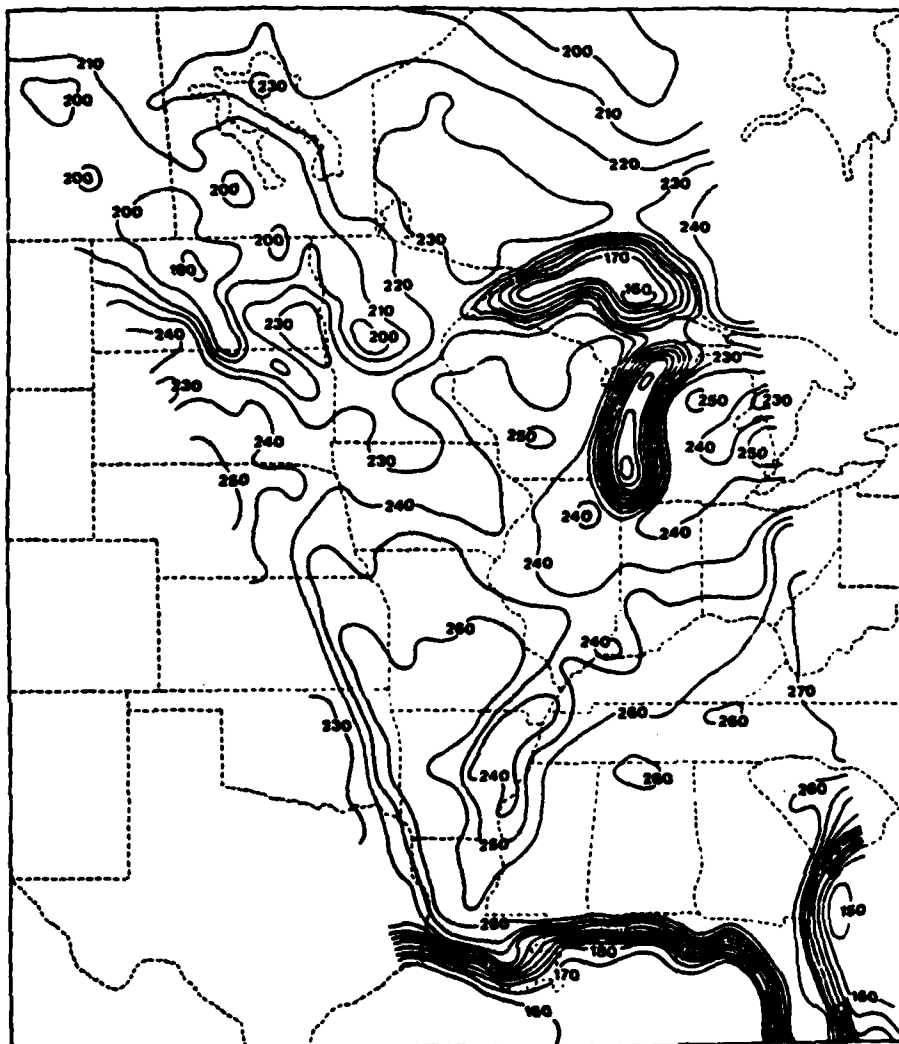


Figure 4.6. Average microwave brightness temperature ($^{\circ}\text{K}$) from the horizontally and vertically polarized components of ESMR. These data were obtained from orbit 3397 of Nimbus VI on 20 February 1976 at 1710 GMT.

significant variations in average brightness temperatures over land in the 0.81 cm wavelength region of ESMR are present in relatively cloud free areas. Values of T_{AVG} were less than $240^{\circ}K$ along the Mississippi River Valley in eastern Arkansas and were associated with wet soil conditions where 24 hour rainfall amounts exceeded 1 inch on the previous day. Dry soil conditions were present over Alabama and Georgia where $T_{AVG} > 260^{\circ}K$. Colder brightness temperatures ($< 200^{\circ}K$) were present over North Dakota and southern Canada where there was snow cover.

Percentage polarization of the horizontal and vertical brightness temperature components of ESMR as defined in Eq. 2.3 is shown in Fig. 4.7. Even though the values were small and amounted to less than 7% over land areas, there were variations in the polarization field that were related to different surface conditions that were also noted in Fig. 4.6. The wet soil conditions along the lower Mississippi Valley were related to areas where $P\% > 4\%$ while the dry soil in Alabama and Georgia was associated with $P\% < 2\%$. Snow covered areas further north coincided with polarization values in excess of 5%. Another area, where $P\% > 4\%$, was located over northern Iowa and was related to precipitation east of the mid-latitude cyclone as shown in the radar summaries in Fig. 2.9. It was likely that the precipitation in this area had been in progress for a sufficient period of time to produce wet soil conditions.

Scattergrams of ESMR and conventional meteorological data are shown in Fig. 4.8 for more than 60 data points obtained from Figs. 4.6 and 4.7 where T_{SFC} data were available from surface observations.

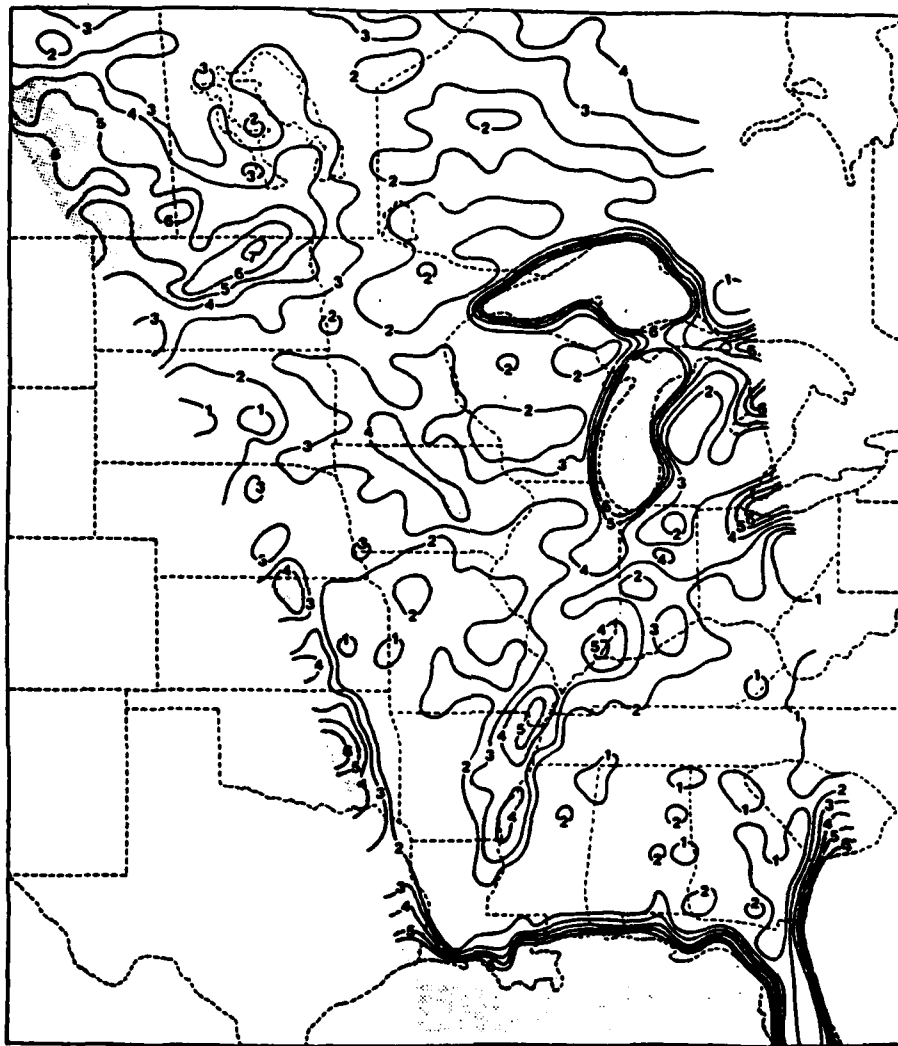


Figure 4.7. Linear polarization expressed as a percentage and defined in Eq. 2.3 for microwave brightness temperature of ESMR. These data were obtained from orbit 3397 of Nimbus VI on 20 February 1976 at 1710 GMT.

The percentage polarization of ESMR brightness temperatures are given for each point on the scattergram. Also, different surface conditions are denoted as well as lines representing constant ratios of T_{AVG}/T_{SFC} to estimate emissivities of T_{AVG} .

It is evident from Fig. 4.8 that the microwave brightness temperatures were generally more than 30°K less than the conventional surface temperatures. For percentage polarizations less than 2%, the estimated emissivities were approximately 0.90. These data points represented mostly dry soil conditions. For higher percentage polarization values ($P\% > 3\%$) the estimated emissivities tended to be less than 0.85. The two points with the highest percentage polarizations (5%) were associated with snow cover and had estimated emissivities of less than 0.80 as shown in Fig. 4.8. It is clearly evident that the ESMR measurements over land were dependent on surface conditions.

Radiance values of reflected solar radiation from channel 17 of HIRS and shown in Fig. 2.6b are plotted in Fig. 4.9 with respect to T_{IR} values from HIRS (Fig. 2.6a) and T_{AVG} from ESMR for the corresponding data points shown in Fig. 4.8. It is evident from this scattergram that data points tended to be clustered with respect to similar surface and cloud conditions. For example, small radiance values ($\leq 5 \text{ ergs s}^{-1}/\text{cm}^{-1}$) were associated with clear cases where T_{IR} values exceeded 280°K. At these warm infrared temperatures, dry soil cases with clear skies were associated with T_{AVG} values around 260°K and $T_{AVG}/T_{IR} \approx 0.90$ while moist soil cases were clustered near $T_{AVG} = 240^\circ\text{K}$ and $T_{AVG}/T_{IR} \approx 0.85$.

Comparison of the GOES visible and infrared satellite images in

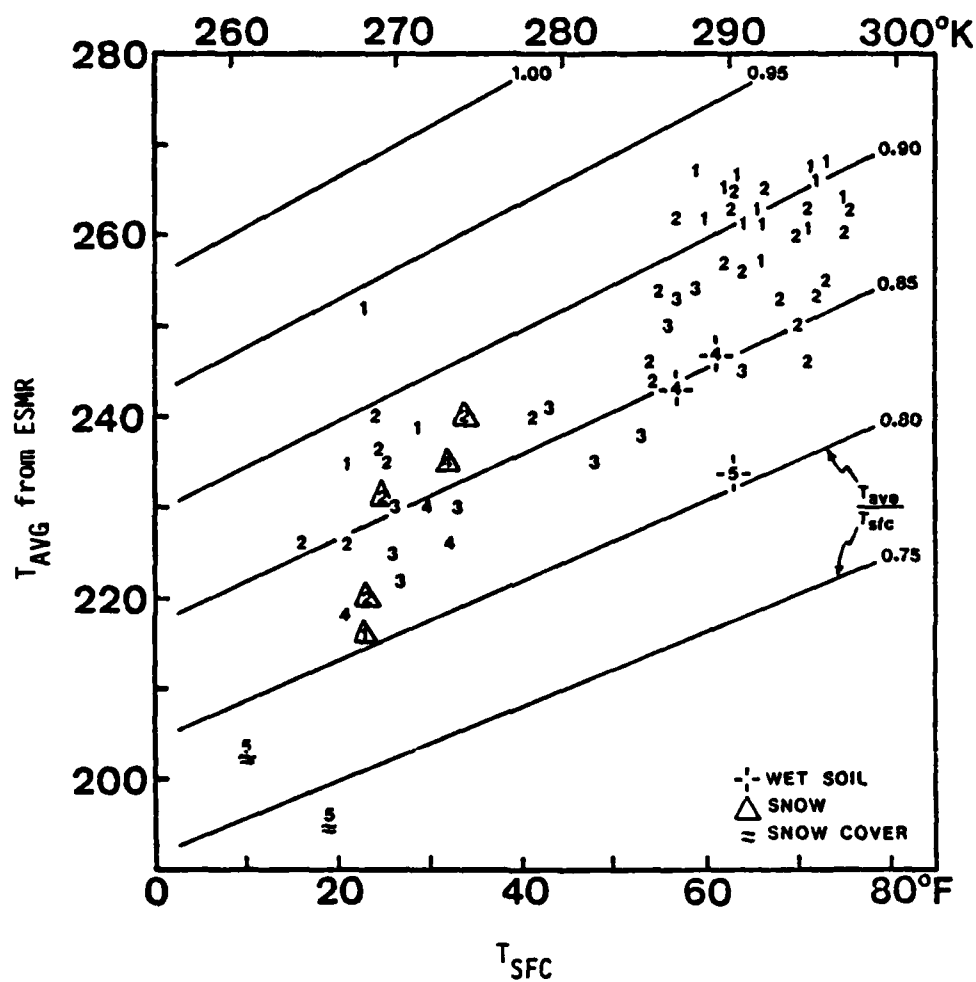


Figure 4.8. Percentage polarization of ESMR microwave brightness temperature plotted with respect to ESMR average brightness temperature and conventional surface temperature for 20 February 1976. Lines representing $T_{\text{AVG}}/T_{\text{SFC}}$ are shown for estimates of emissivities for T_{AVG} .

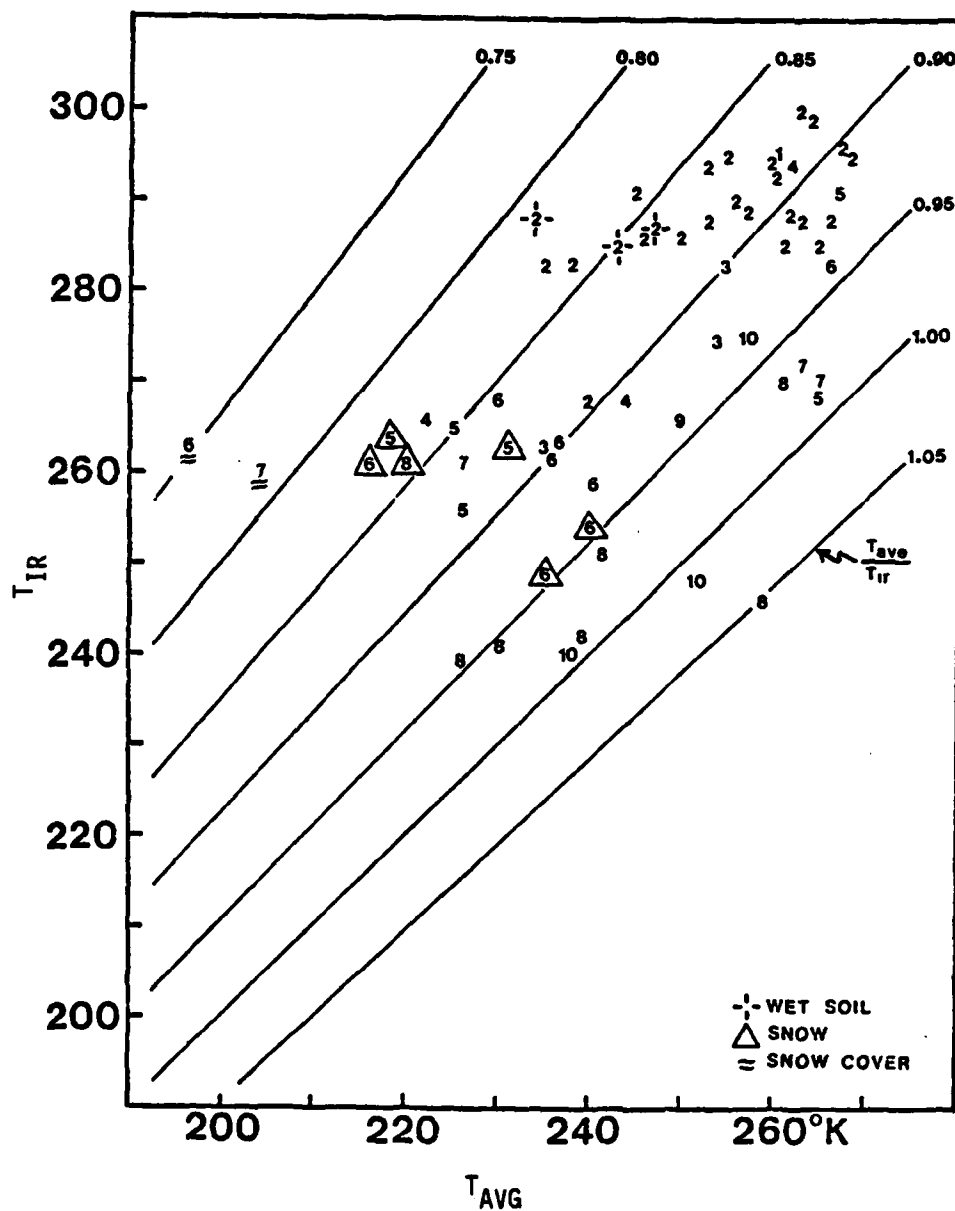


Figure 4.9. Radiance values ($\text{ergs s}^{-1}/\text{cm}^{-1}$) from channel 17 of HIRS plotted with respect to infrared temperature from HIRS and average brightness temperature from ESMR for 20 February 1976. The ratio of different values of T_{AVG}/T_{IR} are indicated in comparisons.

Figs. 2.11 and 2.12 with reflected solar radiation shown in Fig. 2.6b indicated overcast skies were present whenever radiance values exceeded $7.5 \text{ ergs s}^{-1}/\text{cm}^{-1}$. These points were easily identified in the scattergram in Fig. 4.9 where T_{IR} values were generally less than 270°K . Values of $T_{\text{AVG}}/T_{\text{IR}}$ that exceeded 1.0 were associated with high overcast cloud conditions where cloud top temperatures were very cold. Values less than 0.80 for $T_{\text{AVG}}/T_{\text{IR}}$ were associated with two data points where snow cover conditions with clear skies resulted in high reflected solar radiances but low temperature values for both T_{IR} and T_{AVG} . This scattergram supports the results shown in Tables 4.16 and 4.17 which compared microwave measurements with the infrared and solar radiation from HIRS.

CHAPTER V

SUMMARY

In this study it was shown that the Nimbus VI SCAMS temperature retrieval channels were sensitive to surface moisture and precipitation. Linear correlation coefficients obtained between SCAMS and conventional surface temperature measurements showed somewhat higher values or better correlations for precipitation cases than for clear sky cases. This result may be unique to this particular wintertime synoptic system and further studies are required in order to formulate a physical explanation of the correlative information. Low level overcast clouds contributed to more variations in the SCAMS water vapor and window temperature retrieval channels than did high level atmospheric moisture as higher correlation coefficients were obtained for overcast low cloud than for overcast high cloud conditions. Also shown was that liquid water content of non-precipitating clouds somewhat degraded satellite temperature retrievals at mid-tropospheric levels. Multiple correlation coefficient results indicated that more accurate temperature measurements were not possible in precipitating cloud over land areas at the 1.350 and 0.948 cm microwave region from SCAMS measurements.

Terrain elevations also significantly effected SCAMS temperature retrievals. For elevations above 1000 meters very low surface temperature correlations coefficients were obtained, which can in part be

attributed to snow cover over mountain regions. SCAMS measurements were also found to be sensitive to diurnal soil temperature fluctuations which may be significantly different from the overlying surface air temperatures obtained from standard instrument shelters observations.

Comparisons of SCAMS, ESMR and conventional temperature retrievals showed very high correlations for clear sky dry soil conditions where surface emissivities in the microwave regions were very high. For cases of overcast conditions at various atmospheric levels the correlation coefficient results showed that ESMR wavelengths were not significantly affected by atmospheric moisture and that lower correlation coefficients obtained were due to moist soil conditions where emissivities were lower. Interestingly, a large difference between the vertically and horizontally polarized ESMR channels and conventional surface temperature correlation coefficients for low, low and middle cloud condition existed. ESMR's vertically polarized channel with conventional surface temperature measurements revealed substantially more correlated information than with the horizontally polarized channel and may be attributed to polarization of wet soil and snow cover rather than clouds. Terrain heights and its effects on ESMR was attributed to wintertime snow cover with variable radiative characteristics over the mountain areas.

HIRS infrared and reflectance channel data were correlated with SCAMS, ESMR and conventional obtained temperatures. High correlation coefficients were obtained for clear sky cases between HIRS and conventional SCAMS and ESMR surface temperature measurements and low values for overcast conditions, as expected, due to HIRS sensitivity to surface or cloud top temperatures. Correlations of SCAMS surface

temperatures with HIRS solar reflectance showed small negative correlations indicative of cases with low albedoes as over cloud free, dry soil areas and lower correlations resulted for cloud free, wet soil areas.

These results provide important information about multispectral sensing of a wintertime mid-latitude cyclone over land and need to be extended to include other types of synoptic systems which occur during other seasons. Also, these results establish useful statistical computations which can be used to develop algorithms for remote sensing of surface and atmospheric moisture parameters.

APPENDIX A

THE DATA

The parameters in the data set for this study are listed here.

Parameters 1 to 26 are identified below.

1. Station number
2. Station identifier
3. T_{B1}
4. T_{B2}
5. T_{B3}
6. T_{B4}
7. T_{B5}
8. T_{SFC}
9. RH_{SFC}
10. RH_{500}
11. T_{500}
12. T_{500S}
13. T_{1000S}
14. Cloud type group: low, middle, high (0-no, 1-yes)
15. Cloud amount (0-clear, 1-scattered, 2-broken, 3-overcast, 4-obscured)
16. Precipitation observed (0-no, 1-yes)
17. Precipitation radar (0-no, 1-yes)
18. No-precipitation radar (0-no, 1-yes)

- 19. No-precipitation observed (0-no, 1-yes)
- 20. Visibility restriction: 0-unrestricted
1-haze
2-smoke
3-fog
4-dust
5-rain
6-snow
7-ice crystals
8-thunderstorm
- 21. TER
- 22. Time increment
- 23. T_B^h
- 24. T_B^v
- 25. T_{IR}
- 26. REFL

Notes: 1) For clear sky cases data parameters 16 - 19 are identified as all 0's.

2) Parameters 1 - 13, 21, and 23 - 26 are defined in Table 3.1.

[illegible]

[illegible]

APPENDIX B

SAMPLE CORRELATION COEFFICIENT ARRAYS

Correlation coefficients for the overcast high cloud only cases are presented to show an example of the computational output. Samples B.1, B.3 and B.5 represent arrays of linear correlations that were computed from Eq. 3.1. Arrays B.2, B.4 and B.6 represent output computations of the multiple correlations obtained from Eq. 3.2. Individual parameters in the correlation coefficients can be identified from the following list and correspond to each row and column sequentially in the arrays.

1. T_{B1}
2. T_{B2}
3. T_{B3}
4. T_{B4}
5. T_{B5}
6. T_{SFC}
7. RH_{SFC}
8. RH_{500}
9. T_{500}
10. T_{500S}
11. T_{1000S}
12. Cloud
13. Terrain

14. T_B^h (ESMR)
15. T_B^v (ESMR)
16. T_{IR} (HIRS)
17. Radiance (Reflectance - HIRS)
18. T_{AVG} (ESMR)
19. Percent polarization (ESMR)

The number beneath the linear coefficient array T_{B2} column identifies the number of cases correlated.

The T_{B1} multiple correlations coefficient sample array according to Eq. 3.2 was selected for B.2, B.4 and B.6, i.e.

$$R^2 = [T_{B1}(x_j, x_i)]$$

B.1. Sample of SCAMS/Conventional Linear Correlation Coefficients.

	1	2	3	4	5	6	7	8	9	10	11	12	13
1	1.0000	.9708	-.8728	.7044	-.6392	-.6570	-.0454	.1328	.7282	.7557	.4317	.0091	-.2345
2	.9708	1.0000	-.8657	.6794	-.5872	-.6359	-.0141	.1255	.7353	.7308	.4396	.0064	-.2625
3	-.8728	-.8657	1.0000	-.9215	-.6618	-.6722	-.0518	.0389	.4303	.4252	.5133	.0134	-.2940
4	.7044	.6794	-.9215	1.0000	-.4091	.5587	-.0022	.0251	.7018	.7247	.4633	.0352	-.2249
5	-.6392	-.5872	-.6618	-.4091	1.0000	-.4921	.2131	.1142	-.7334	-.8854	-.4208	.0371	-.0532
6	.6570	.6359	-.6722	.5587	-.4921	1.0000	-.1019	.1448	.7251	.6373	.5235	.0111	-.2760
7	-.0454	-.0141	-.0518	-.0022	.2131	-.1019	1.0000	-.0591	-.0875	-.2284	-.2193	.0016	-.3835
8	.1328	.1255	.0389	.0251	.1142	.1448	-.0591	1.0000	.0947	.0126	.1061	.0006	-.0784
9	.7282	.7353	.4303	.7018	-.7334	.7251	-.0875	.0947	1.0000	.8519	.5638	.0166	-.1206
10	.7557	.7308	.4396	.7247	-.8854	.6373	-.2284	.0126	.4519	1.0000	.6522	.0183	.1712
11	.4317	.4396	.5133	.4633	-.4208	.5235	-.2193	.1061	.5638	.6522	1.0000	.0100	.1963
12	.0091	.0064	.0134	.0352	.0371	.0111	.0006	.0006	.0166	.0183	.0100	1.0000	.0004
13	-.2345	-.2625	-.2940	-.2249	-.0532	-.2740	-.3835	-.0784	-.1206	.1712	.1963	.0004	1.0000

B.2. Sample of SCAMS/Conventional Multiple Correlation Coefficients for

$$R^2 = [T_{B1}(x_j, x_i)].$$

	1	2	3	4	5	6	7	8	9	10	11	12	13
1	.000	.000	.000	.000	.000	.000	.000	.000	.000	.000	.000	.000	.000
2	1.000	1.000	.704	.497	.428	.432	.018	.018	.544	.571	.194	.000	.076
3	1.000	.944	1.000	.891	.454	.491	.003	.043	.649	.446	.265	.000	.089
4	1.000	.943	.948	1.000	.413	.450	.003	.027	.601	.645	.237	.001	.063
5	1.000	.944	.780	.500	1.000	.440	.059	.045	.652	.747	.226	.003	.125
6	1.000	.943	.787	.512	.418	1.000	.011	.034	.637	.606	.288	.000	.081
7	1.000	.943	.762	.497	.442	.437	1.000	.020	.533	.609	.226	.000	.211
8	1.000	.943	.768	.501	.449	.441	.005	1.000	.530	.579	.189	.000	.057
9	1.000	.944	.843	.572	.561	.561	.008	.018	1.000	.765	.319	.000	.060
10	1.000	.943	.620	.562	.651	.478	.090	.036	.742	1.000	.434	.000	.338
11	1.000	.943	.785	.527	.438	.502	.051	.021	.607	.702	1.000	.000	.164
12	1.000	.943	.762	.497	.410	.432	.002	.018	.530	.571	.186	1.000	.055
13	1.000	.944	.770	.500	.452	.447	.166	.020	.533	.699	.280	.000	1.000

B.3. Sample of SCAMS/Conventional/ESMR Linear Correlation Coefficients.

	1	2	3	4	5	6	7	8	9	10	11	12	13	14	15	16	17	18	19
1	1.000	.908	.914	.917	.695	.003	-.620	.034	.011	.005	.717	.018	-.463	.463	.749	.000	.000	.589	.013
2	.908	1.000	.802	.756	-.644	.071	-.604	.022	.745	.829	.629	.016	-.402	.401	.745	.000	.000	.590	-.026
3	.914	.802	1.000	.959	-.708	.053	-.518	-.003	.671	.894	.753	.030	-.625	.460	.747	.000	.000	.586	.013
4	.917	.756	.959	1.000	-.756	.763	-.417	.017	.859	.879	.789	.045	-.580	.394	.668	.000	.000	.513	.047
5	.695	-.644	-.708	-.756	1.000	-.686	.539	.225	-.900	-.773	.642	.009	.489	-.059	-.430	.000	.000	-.212	-.405
6	.003	.071	.053	.763	.686	1.000	-.509	.003	.000	.844	.713	.037	-.395	.412	.703	.000	.000	.539	.048
7	-.620	-.609	-.518	-.417	.539	-.509	1.000	.017	-.548	-.476	.432	.004	.172	-.037	-.285	.000	.000	-.137	-.201
8	.034	.022	-.003	.017	.225	.003	.017	1.000	-.070	-.094	.079	.001	.080	-.196	-.271	.000	.000	-.231	.078
9	.011	.745	.671	.859	-.900	.808	-.548	-.070	1.000	.919	.815	.041	-.410	.178	.544	.000	.000	.328	.311
10	.005	.829	.629	.745	.894	.753	.030	.671	.894	1.000	.922	.041	-.286	.395	.715	.000	.000	.533	.036
11	.717	.629	.753	.789	-.642	.713	-.432	-.073	.815	.922	1.000	.040	-.017	.437	.682	.000	.000	.546	-.027
12	.018	.016	.030	.045	.089	.037	.004	.001	.041	.041	.048	1.000	.001	.009	.015	.000	.000	.012	.001
13	-.463	-.442	-.625	-.580	.689	-.395	.172	.000	-.430	-.286	.017	.001	1.000	-.014	-.190	.000	.000	-.048	-.214
14	.463	.441	.460	.394	-.059	.412	-.037	.106	.178	.305	.437	.009	.009	1.000	.097	.000	.000	.944	-.850
15	.749	.745	.747	.668	-.439	.703	-.285	-.271	.544	.715	.682	.015	-.158	.097	1.000	.000	.000	.961	-.531
16	.000	.000	.000	.000	.000	.000	.000	.000	.000	.000	.000	.000	.000	.000	.000	.000	.000	.000	.000
17	.000	.000	.000	.000	.000	.000	.000	.000	.000	.000	.000	.000	.000	.000	.000	.000	.000	.000	.000
18	.589	.598	.586	.513	-.212	.539	-.137	-.231	.328	.533	.546	.012	-.088	.984	.961	.000	.000	1.000	-.744
19	.013	-.026	.013	.047	-.405	.048	-.201	.078	.311	.096	-.027	.001	-.214	-.050	-.531	.000	.000	-.744	1.000

B.4. Sample of SCAMS/Conventional/ESMR Multiple Correlation Coefficients

$$R^2 = [T_{B1}(x_j, x_i)]$$

1	2	3	4	5	6	7	8	9	10	11	12	13	14	15	16	17	18	19
1	.000	.000	.000	.000	.000	.000	.000	.000	.000	.000	.000	.000	.000	.000	.000	.000	.000	.000
2	1.000	1.000	.854	.774	.561	.781	.385	.007	.792	.868	.771	.000	.237	.561	.000	.000	.000	.000
3	1.000	.970	1.000	.942	.624	.793	.399	.081	.760	.827	.572	.001	.463	.584	.000	.000	.361	.000
4	1.000	.854	.971	1.000	.590	.786	.409	.082	.774	.856	.638	.003	.334	.570	.000	.000	.350	.000
5	1.000	.974	.880	.736	1.000	.790	.407	.121	.807	.831	.554	.020	.268	.549	.000	.000	.422	.303
6	1.000	.976	.845	.675	.507	1.000	.392	.085	.696	.803	.543	.002	.215	.568	.000	.000	.444	.006
7	1.000	.976	.840	.680	.503	.783	1.000	.004	.661	.791	.514	.001	.236	.612	.000	.000	.431	.121
8	1.000	.974	.849	.667	.546	.781	.386	1.000	.668	.790	.525	.000	.223	.648	.000	.000	.410	.086
9	1.000	.985	.885	.780	.629	.805	.391	.029	1.000	.901	.673	.002	.217	.572	.000	.000	.412	.264
10	1.000	.985	.869	.780	.594	.801	.409	.037	.843	1.000	.896	.003	.284	.573	.000	.000	.347	.033
11	1.000	.989	.855	.752	.526	.793	.385	.023	.770	.953	1.000	.003	.417	.604	.000	.000	.378	.003
12	1.000	.976	.836	.668	.494	.781	.385	.001	.659	.783	.515	1.000	.214	.560	.000	.000	.347	.000
13	1.000	.977	.838	.719	.519	.781	.402	.013	.650	.802	.640	.000	1.000	.588	.000	.000	.390	.055
14	1.000	.977	.837	.660	.577	.780	.465	.059	.704	.783	.524	.000	.265	.904	.000	.000	.991	.437
15	1.000	.976	.845	.675	.599	.784	.458	.201	.667	.789	.562	.000	.264	1.000	.000	.000	.962	.664
16	1.000	.976	.836	.667	.484	.780	.385	.001	.658	.783	.514	.000	.214	.560	.000	.000	.947	.000
17	1.000	.974	.836	.667	.544	.780	.385	.001	.658	.783	.514	.000	.214	.560	.000	.000	.947	.000
18	1.000	.974	.839	.664	.543	.781	.465	.034	.682	.783	.537	.000	.264	.990	.000	.000	1.000	.465
19	1.000	.977	.836	.664	.480	.782	.459	.007	.748	.790	.515	.000	.257	.947	.852	.000	.912	1.000

B.6. Sample of SCAMS/Conventional/HIRS Multiple Correlation Coefficients

$$R^2 = [T_{B1}(x_j, x_i)].$$

1	1	2	3	4	5	6	7	8	9	10	11	12	13	14	15	16	17	18	19
1	1.000	.000	.000	.000	.000	.000	.000	.000	.000	.000	.000	.000	.000	.000	.000	.000	.000	.000	.000
2	1.000	1.000	.721	.523	.571	.704	.701	.015	.000	.619	.543	.000	.000	.000	.000	.000	.000	.000	.000
3	1.000	.967	1.000	.947	.769	.726	.761	.030	.033	.000	.468	.001	.000	.000	.000	.000	.000	.000	.000
4	1.000	.963	.965	1.000	.750	.661	.761	.018	.000	.000	.450	.002	.000	.000	.000	.000	.000	.000	.000
5	1.000	.963	.931	.723	1.000	.516	.769	.053	.000	.000	.350	.024	.000	.000	.000	.000	.000	.000	.000
6	1.000	.961	.844	.715	.633	1.000	.765	.044	.000	.000	.712	.001	.000	.000	.000	.000	.000	.000	.000
7	1.000	.962	.683	.517	.590	.431	1.000	.066	.000	.000	.297	.001	.000	.000	.000	.000	.000	.000	.000
8	1.000	.962	.686	.517	.580	.442	.791	1.000	.000	.000	.322	.000	.000	.000	.000	.000	.000	.000	.000
9	1.000	.969	.917	.841	.785	.702	.777	.014	1.000	.000	.566	.001	.000	.000	.000	.000	.000	.000	.000
10	1.000	.967	.884	.823	.702	.701	.754	.014	.000	1.000	.593	.001	.000	.000	.000	.000	.000	.000	.000
11	1.000	.974	.764	.632	.594	.771	.776	.076	.617	.753	1.000	.000	.000	.000	.000	.000	.000	.000	.000
12	1.000	.962	.881	.716	.573	.825	.754	.014	.362	.561	.276	1.000	.000	.000	.000	.000	.000	.000	.000
13	1.000	.963	.793	.629	.736	.843	.796	.105	.000	.563	.279	.000	1.000	.000	.000	.000	.000	.000	.000
14	1.000	.964	.822	.696	.705	.727	.708	.022	.000	.746	.347	.000	.000	.000	.000	.000	.000	.000	.000
15	1.000	.963	.683	.516	.571	.844	.701	.227	.369	.561	.496	.000	.152	.000	.000	.000	.000	.000	.000
16	1.000	.967	.707	.554	.583	.830	.761	.231	.364	.561	.341	.000	.247	.000	.000	1.000	.000	.000	.000
17	1.000	.963	.681	.524	.580	.804	.745	.300	.000	.637	.360	.000	.150	.000	.000	.000	.767	1.000	.000
18	1.000	.962	.681	.516	.563	.824	.754	.014	.361	.561	.276	.000	.094	.000	.000	.000	.537	.232	.000
19	1.000	.962	.681	.516	.563	.824	.754	.014	.361	.561	.276	.000	.094	.000	.000	.000	.537	.232	.000

REFERENCES

- Astling, E. G. and K. N. Liou, 1979: Analyze, calculate and develop techniques for weather satellite imagery data. AFGL-TR-79-0140, Air Force Geophysics Laboratory, United States Air Force, Hanscom AFB, Massachusetts, 126.
- Corbell, R. P., C. J. Callahan, and W. J. Kotsch, Editors, 1977: GOES/SMS User's Guide, NOAA/NASA Publication, Washington, D. C., 118 pp.
- Cressman, G. P., 1959: An operation objective analysis system. Mon. Wea. Rev., 87, 367-374.
- Geiger, R., 1965: The climate near the ground, Harvard University Press. 611.
- Grody, N. C. and P. P. Pellegrino, 1977: Synoptic-scale studies using the Nimbus VI scanning microwave spectrometer. J. Appl. Meteor., 16, 816-826.
- Hall, J. A., 1979: A dynamic and synoptic study of a wintertime cyclone using geostationary and polar orbiting satellite data. Masters Thesis, University of Utah, Salt Lake City, Utah, 84.
- Hayden, C. M., 1979: Remote soundings of temperature and moisture. Quantitative Meteorological Data from Satellites. World Meteorological Organization Technical Note No. 166, Geneva, Switzerland, 32.
- Kern, C. D., 1963: Desert soil temperatures and infrared radiation received by Tiros III. J. Atmos. Sci., 20, 175-176.
- Peyrefitte, A. G., and E. G. Astling, 1980: Mapping snow cover over the western United States with microwave brightness temperatures from Nimbus VI ESMR experiment. Paper in preparation.
- Rogers, E., H. Siodalingaiah, A. T. C. Chang and T. Wilheit, 1979: A statistical technique for determining rainfall. J. Appl. Meteor., 18, 978-991
- Staelin, D. H., A. H. Barrett, P. W. Rosenkranz, F. T. Barath, E. J. Johnson, J. W. Waters, A. Wouters and W. B. Lenoir, 1975: The scanning microwave spectrometer (SCAMS) experiment. Nimbus VI Users Guide, Goddard Space Flight Center, Greenbelt, Md.

Staff Members, 1975: Nimbus VI User's Guide, Goddard Space Flight Center, NASA, Md. p 227.

Tvewaratha, G. T., 1954: An introduction to climate. McGraw-Hill Book Company, Inc., 402.

Weinman, J. A. and P. J. Guetter, 1977: Determination of rainfall distributions from microwave radiation measured by the Nimbus VI ESMR. J. Appl. Meteor., 16, 437-442.

Wilhett, T. T., J. S. Theon, W. E. Shenk and L. J. Allison, 1976: Meteorological interpretations of the images from the Nimbus V electrically scanned microwave radiometer. J. Appl. Meteor., 15, 166-172.

VITA

Name	Peter Werner Speck
Birthdate	September 21, 1943
Birthplace	Langengrassau, Germany
High School	Mainland High School Daytona Beach, Florida
Universities	
1967-1970	Brevard Community College Cocoa, Florida
1968-1972	Rollins College Winter Park, Florida
1972-1974	Saint Louis University Saint Louis, Missouri
1978-1980	University of Utah Salt Lake City, Utah
Degree	
1974	B.S., Saint Louis University
Honorary Societies	Chi Epsilon Phi
Professional Position	Weather Officer United States Air Force